UNIVERSITY OF TWENTE.

**Faculty of Electrical Engineering,
Mathematics & Computer Science**

Investigate an optical readout method for a micro Coriolis mass flow sensor

**Qi Wu
M.Sc. Thesis
July 2021**

Supervisors:
dr. ir. R. J. Wiegerink
A. Sundararajan

Integrated Devices and Systems Group
Faculty of Electrical Engineering,
Mathematics and Computer Science
University of Twente
P.O. Box 217
7500 AE Enschede
The Netherlands

Preface

This master's thesis project is based on the Coriolis mass flow sensor developed by the University of Twente and Bronkhorst High-Tech BV, to design and verify the feasibility of an optical reading system based on double grating diffraction.

The project started in January 2021 and lasted for 28 weeks. During this period, dr. ir. R. J. Wiegerink and the Integrated Devices and Systems group provided a good experimental environment and technical support for me to ensure the smooth progress of the research tasks. As my daily supervisor, A. Sundarajan provided sufficient practical guidance and advice. Their support and efforts helped me successfully break through many bottlenecks one after another. Here, I would like to express my sincerest gratitude to them.

In the research process of this thesis, I consolidated the theoretical knowledge related to semiconductors technology that I learned before, and studied the knowledge related to optical diffraction in depth. At the same time, I also gained more valuable experience on how to research problems, solve problems, and even ask for help. This experience is of far-reaching significance for my subsequent academic development.

For now, my M.Sc program is about to finish. Thanks to my parents for their financial support for my two years of study and life. I hope my little shining can be the one you proud of.

Qi Wu

July 2021

Summary

With the rapid replacement of semiconductor sensor devices, the overall device size continues to shrink. As a sensitive component, the structure usually has micrometer or even nanometer displacement that needs to be accurately measured. The small displacement detection method with high sensitivity and excellent dynamic response is facing challenges.

The purpose of this paper is to design and verify an optical displacement readout system for a micro Coriolis mass flow sensor. The target to be detected is an integrated suspended micro-tube, with millimeter size dimensions and nanometer level out-of-plane displacements. We designed the top surface of the micro-tube as a reflecting mirror, and set a fixed grating above it to form a double grating diffraction structure. Based on the theory of grating diffraction, the diffracted order intensity of the composite diffracted light field is sensitive to the displacement of the mirror surface, and the light sensor can be used to convert the detectable light signal into an electrical signal.

In this report, the working principle of this double grating diffraction based readout system is theoretically deduced and a mathematical model is established. Through optical simulation and numerical calculation, it is verified that the detection range of this system meets the requirements of the flow sensor. At the same time, due to the periodicity of the motion pattern of the movable micro-tube, the phase shift analysis method was adopted and high sensitivity ($0.03 rad/nm$) was reached.

Based on theoretical research, the related devices selection and layout design of the optical readout system have also been completed. A series of preliminary experiments confirmed that the light signal changes caused by the nano-scale periodic motion can be detected and measured.

The thesis initially verified the feasibility of the designed optical reading system, and the actual sensitivity and dynamic performance still require subsequent device fabrication and testing.

Contents

List of acronyms

MEMS   microelectromechanical systems

CCD   charge-coupled device

SiRN   silicon-rich silicon nitride

LPCVD   low-pressure chemical vapor deposition

RIE   reactive ion etching

DRIE   deep reactive ion etching

VCSEL   vertical-cavity surface-emitting laser

GUI   graphical user interface

PDs   photo-detectors

FDTD   finite-difference time-domain

EEL   edge-emitting laser

SMD   surface mount component

EM fields   electric and magnetic fields

FFT   Fast Fourier Transform

SCT   Surface Channel Technology

Chapter 1

Introduction

1.1 Introduction of micro Coriolis flow sensor

This thesis is based on the micro Coriolis mass flow sensor developed by Bronkhorst, an advanced sensor manufacturer focusing on low flow fluidics handling technology. The sensitive part of this flow sensor is a rectangle-shaped suspended microchannel [1], as shown in the Figure 1.1. The fabrication process of the sensor is based on the Surface Channel Technology (SCT) proposed in [2], [3]. Firstly, a layer of a low-stress silicon-rich silicon nitride (SiRN) (thickness: $500nm$) layer is deposited on the silicon substrate, with slits as the etching windows for the microchannel. The deep reactive ion etching (DRIE) is used to prepare channel on the silicon substrate. The cross section of the channel is circular, and the transmission direction is arranged as a rectangular loop. The second silicon rich nitride layer is deposited by low-pressure chemical vapor deposition (LPCVD). The conformal selectivity of LPCVD deposition contributes to the uniform thickness of sidewalls and sealing of the slits. Finally, the protective silicon rich nitride layers and the silicon substrate are processed by reactive ion etching (RIE) and wet etching, respectively, and the silicon rich nitride micro-tube is released and suspended in the cavity.

 Metal layers deposited as the final process, which will be used as actuation tracks
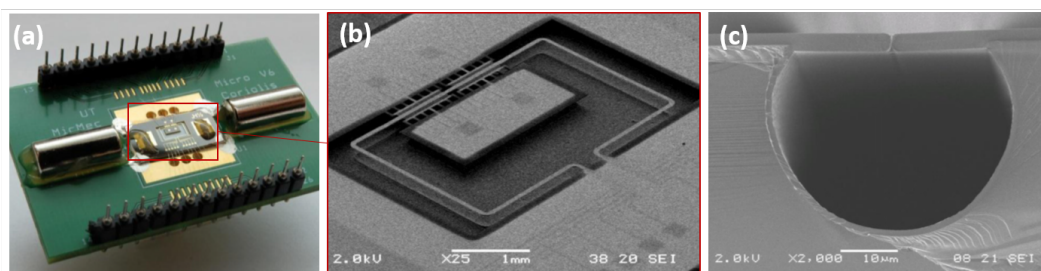
Figure 1.1: (a) The picture of Coriolis mass flow sensor, (b) The SEM figure of the sensing part, (c) Cross section of the suspended micro-tube.

for the sensor. So that, under the influence of the external stable magnetic field and alternating current, the tube is driven by Lorentz force to make periodic motion. According to the simulations from the previous research, the micro-tube can have two types of motion depending on the driving frequency [4]. As shown by the eigenfrequency simulation calculation results, Figure 1.2, when the driving frequency is close to $1.3kHz$, the direction of movement of the tube along the x-axis on both sides is the same. When the driving frequency is increased to $2.3kHz$, the tubes on both sides move in opposite directions. These two initial actuation modes can be called Swing mode and Twist mode, respectively.

When the micro-tube is in a Twist mode, the y-axis parallel segment rotates around
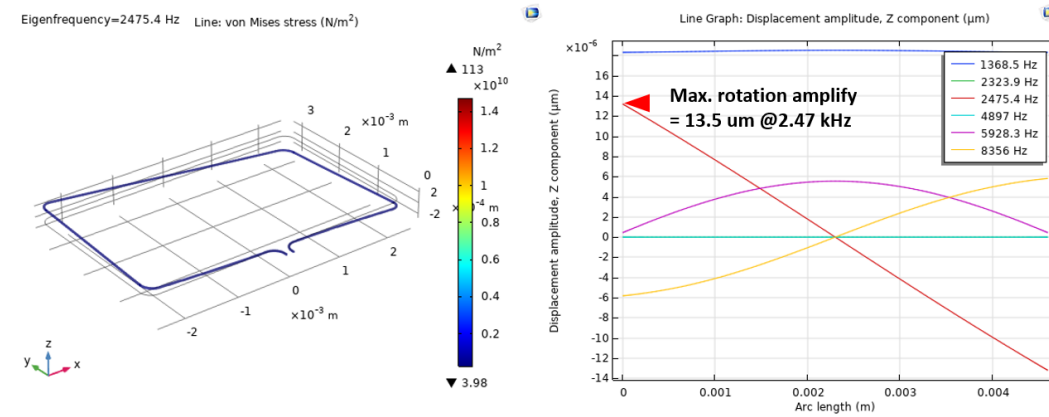
Figure 1.2: Comsol eigenfrequency test results, showing the front-segment tube vertical displacements with different driven frequencies.

the central axis of the plane. At this time, the mass flow passes through the tube, the mass unit has two orthogonal motions, including forward movement through the tube and rotational movement with the tube. As the result, mass flow will be affected by the Coriolis force. Coriolis force is an effect produced by the inertia of an object, which can be determined and calculated by a vector Equation (1.1).

$$\overrightarrow{F_c} = -2 \cdot L_y \cdot \left(\overrightarrow{\omega_{am}} \times \overrightarrow{\Phi_m} \right) \tag{1.1}$$

Where L_y is the length of the Coriolis force sensitive part, the y-axis parallel segment in this case. ω_{am} and Φ_m are the angular velocity and mass flow rate of the moving fluid respectively.

Therefore, when the micro-tube is in a initial Twist mode, Coriolis forces are realized in vertical plane, causing the tube to move vertically, as shown in the Figure 1.3 [2]. So that with the two effects of Lorentz force and Coriolis force the suspended micro-tube always has a compound motion.
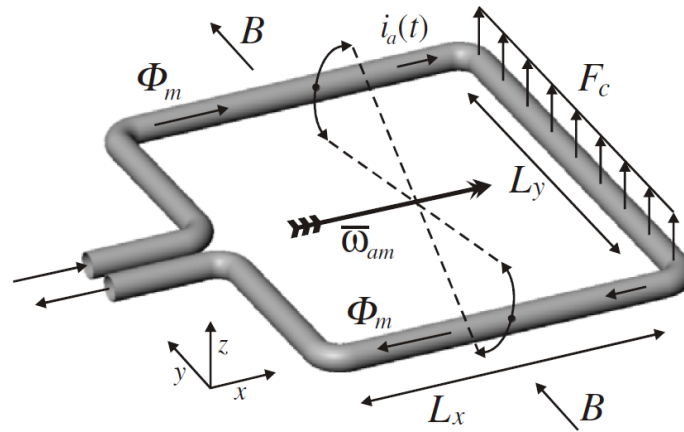
Figure 1.3: The suspended micro-tube in the micro Coriolis flow sensor. The ω_{am} is the actuation-mode angular velocity; F_c indicates the Coriolis force as a result of mass flow [1].

In previous research, the small displacement of this compound motion was measured and characterized by micro system analyzer [2], [3]. The $5mm$ long y-axis parallel segment has an amplitude in the order of $10um$ at the corners of the retangular loop, equivalenting to a rotation of 0.034 degrees. And the Coriolis force can produce displacements up to $100nm$ at the maximum flow rate.. So the range of displacement to be detected is summarized in the Table 1.1.

Table 1.1: Technical parameters of the detection range of the readout system.

Force	Direction	Measurement range
Lorentz force	Rotational	$0 - 0.034$ degrees
Coriolis force	Vertical	$0 - 100nm$

The current displacement measurement solution adopted for this set of Coriolis flow sensors is based on a capacitive detection method. The sensitive part is a set of fixed comb-shape electrodes and another set of movable same shape electrodes connect with the suspended micro-tube. Thus, the tube's displacement can cause a change in effective distance between the capacitor electrodes. Through the capacitance changing signal collected by the detection circuit, the displacement of the micro-tube and the mass flow rate can be calculated.

The maximum sensitivity of this capacitive design is achieved with electrode spacing of $2um$, this has a disadvantage that causes the electrodes to easily collide with each other under the internal or external shocks. Furthermore, in the micro-scale, the electrodes are at risk of attracting and bonding due to static electricity.

Therefore, a solution of using an optical system instead of capacitive measurement was proposed. The original comb-shaped capacitors were replaced with a light-reflective metal tracks, which will produce vertical displacement and rotation with the movement of the suspended micro-tube. By using a fixed laser beam to irradiate this movable reflector, the reflected light will carry the changing optical signal, with respect to the light intensity, which can be collected by the photo-detectors (PDs). Finally, the movement of the suspended micro-tube can be derived. Because this optical measurement method does not directly contact the moving parts, it can avoid the structural collision problem mentioned above. In addition, the system can provide a good dynamic response performance, because the optical detection method does not involve force generation.

In the group's previous research work, a reflective optical reading structure was experimentally verified with good accuracy, resulting in a $\pm 3\sigma$ confidence interval of $6mg/h$ [5]. As shown in the Figure 1.4, this structure uses the detection of the change in the position of the reflected light spot to calculate the displacement of the mirror. Due to the extremely small displacement of the mirror, this structure requires a larger space to set up the optical path to amplify the displacement of the light spot. At the same time, this measurement method requires computer-aided analysis to position the light spot, rather than directly converting it into an electrical signal. These factors are not feasible for on-chip integrated approach. Therefore, based on this, my thesis project will focus on developing and verifying a more suitable towards integrated optical readout system.
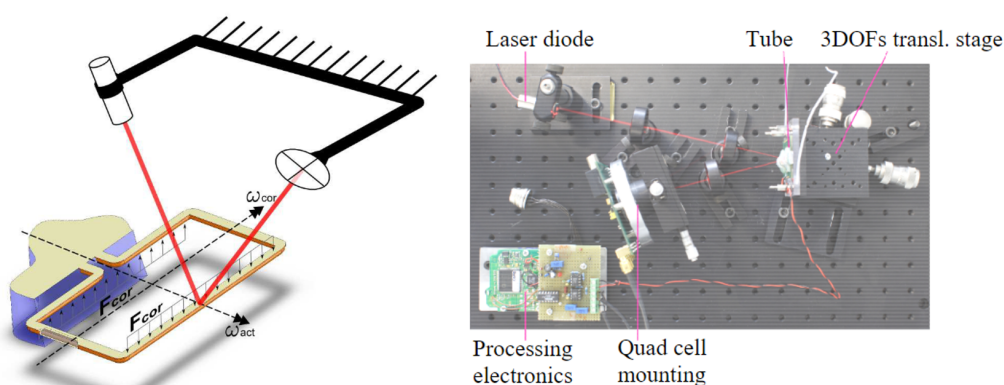
Figure 1.4: The schematic and the measurement setup of the optical system including a quadrant cell light sensor which resolves the spot displacement due to rotational tube deflections.

1.2   Aim of the Thesis

This thesis aims to verify the application of an optical readout method in an existing micro Coriolis flow sensor process. More specifically, a double grating diffraction method is applied with the suspended micro-tube of the sensor. The nano-scaled vertical and rotational displacements of the tube's top-surface influence the diffraction results. The sensing part consists of a vertical-cavity surface-emitting laser (VCSEL) light source and a PDs array to obtain optical signals, which be used to determine the displacement. Finally, the application of this optical detection method is verified and evaluated.

The research work divided and realized the following key contents:

(1) Construct a numerical calculation of double grating diffraction.
    The mathematical model of double grating structure diffraction is derived based on the basic formula of optical diffraction. And through Matlab programming to realize the design of the graphical user interface (GUI). By manually adjusting the parameters, the effects of the grating displacement on the diffraction result can be visualized, and accordingly, it provides a theoretical reference for the system structure and device layout.

(2) Optical simulation of the double grating diffraction.
    In the ANSYS Lumerical, the finite-difference time-domain (FDTD) method is used to optically simulate and verify the conclusions of the mathematical formula, including diffraction grating position, light intensity, and the effects of grating displacements.

(3) Design the layout of the devices and the grating structure.
    Combined with numerical calculation and optical simulation results, the structure and device layout of the overall optical system are comprehensively considered. The key factors included are not limited to optical path medium, working distance (from grating to PDs array), PDs array pitch, waist-width of the laser-beam, etc. According to the design, choose the device's parameters and fabricate the grating with the appropriate process.

(4) Build a testing platform to evaluate the optical measurement methods.
    Considering that integration with existing sensor devices will involve changes in the overall packaging process, a simplified measurement platform was built for experiment. A gold deposited silicon chip is used as a mirror to replicate the top surface of the micro Coriolis tube. This mirror is subjected to periodic displacements. By analyzing the light intensity change signal collected by the PDs array, the displacements of the mirror surface can be monitored. Based

on this, the sensitivity and dynamic response of the optical detection method is verified and evaluated.

1.3   Report organization

The remainder of this report is organized as follows.

In Chapter 2, different solutions for optical detection of small displacement are summarized. By comparing their working principles and performances, the structure of double grating diffraction was selected.

In Chapter 3, the working principle of the double grating based optical readout system is introduced by theory. Firstly, the mathematical model of double grating diffraction is derived. Thus, the distribution position and intensity of the light and dark fringes (diffracted orders) of the diffraction pattern can be calculated. Based on this, by adjusting the tilt angle and relative displacement of the reflective surface in the double grating structure, the corresponding diffraction results can be calculated.

Then, in Chapter 4, through mathematical language programming, the superimposed effects of the two motion modes can be decomposed by analyzing the phase change of the periodic signal. So, the displacement measurement sensitivity can be evaluated theoretically. Next, the double grating diffraction model is developed for optical simulation. The overall structure parameters refer to the previous numerical calculations. The obtained simulation result satisfies the theoretical solutions. So, the theoretical feasibility of the optical readout method is preliminarily proved. Also, the key parameters of each component of this system are summarized to guide subsequent preparation and experimental testing.

In Chapter 5, the construction of the measurement platform and the experimental test results are recorded and summarized. The results verify the feasibility of the optical measurement method. Multiple performances of this sensing system have been evaluated, including sensitivity, dynamic response, stability, etc.

As the end of thesis, in Chapter 6, the report comprehensively summarizes the characteristics of this double grating diffraction based optical measurement method, including the advantages and disadvantages, key influencing factors, and technical/non-technical issues that occurred in the research process. Prospects for the further development of this sort of measurement method are also discussed in the last section.

Chapter 2

Literature review

With the increasing development and improvement of semiconductor processing technology, many devices with micromechanical structures have been developed, including common microelectromechanical systems (MEMS) inertial navigation devices, accelerometers, pressure gauges, microphones, etc. The movable structures contained in these microstructures are usually cantilever beams or elastic films, which are sensitive parts to sense certain input physical quantities or generate corresponding strains on input excitation. Due to the shrinking of the overall size of the device, the amplitude of the displacement of these structures is often limited to the sub-micron order. Determining the sensitivity of detecting small displacements has become a key challenge for improving device performance [6].

The detection methods based on strain gauges or capacitor structures are the most common, benefiting from the mature semiconductor metal layer preparation process [6]–[9]. The small displacement of the device can cause the change of the resistance or capacitance of the sensitive structure, and finally produce a detectable electrical signal. When designing the device structure, factors to be considered, like arranging strain gauges or capacitors reasonably determines the sensitivity of the device. Simultaneously, these sensing structures need to be connected to the original structure of the device, which will have a certain impact on the mechanical characteristics of the overall structure, including intrinsic frequency, quality factor, etc. Therefore, these structures need to be included in device design and dynamic performance analysis.

There are many technologies that can achieve accurate optical displacement measurement. Since there is no physical contact with the structure to be detected, it will not affect the original motion of the structure, and thus has a good dynamic response ability and generally high sensitivity. Industrialized laser displacement sensors generally use two methods: laser triangulation and laser echo analysis [10], [11]. Color confocal and interferometric principles can be used for accurate displacement measurement. In addition, laser displacement sensors are also used for non-contact

7

vibration measurement. Relying on high-quality laser light sources and monitoring cameras and other equipment, such industrialized monitoring devices are difficult to integrate with micro-sensors.

Silicon devices can be processed into complex and fine micron-scale structures through semiconductor technology, which can realize the setting of light sources and the adjustment of light fields in tiny spaces. Optical displacement detection also always frees electrical port for actuation, force feedback operation, and characterization purposes, which is benefit for sensor design [12]. Therefore, the design of the optical reading system has always attracted attention and development. Additional applications include accelerometers, gyroscopes, vibration and pressure sensors, geophones for seismic shooting, photoacoustic gas sensors, and sensors for highly irradiated sites or areas with electromagnetic radiation. The report selected different typical optical measurement methods, and divided them into three categories: reflection type, diffraction type, and double grating diffraction type according to their working principle. The detection performance and application are respectively introduced as follows.

2.1   Optical refraction or reflection

A typical application for optical measurement of small displacement detecting is optical microphones. Commonly such devices have structures that integrates a laser light source and light sensors at the bottom of the cavity, and a reflective membrane is placed above the cavity, which will deform due to sound pressure waves, as shown in the Figure 2.1. Theoperating principle includes flowing steps:

(a) A laser illuminates diffractive lens, a typical component used to separate and focus specific wavelength.

(b) The light passing through the lens is reflected by the microphone membrane and focused on the light detector. The light intensity of the focal point is measured.

(c) When the input acoustic pressure wave causes the membrane to vibrate vertically, the focused light path change. Therefore, the light intensity at the focal point will change and be mapped to the vibration amplitude.

Compared with the capacitance detection based microphone, the structure is simpler, which is feasible for ultra-large-scale production with lower cost [13]. Simultaneously, since the signals of the two light sensor devices are used for comparison, noise can be effectively reduced.

In order to detect the vertical displacement and tilt of the movable part more accurately, the researchers form Kyushu University distributed the light sensors sym-
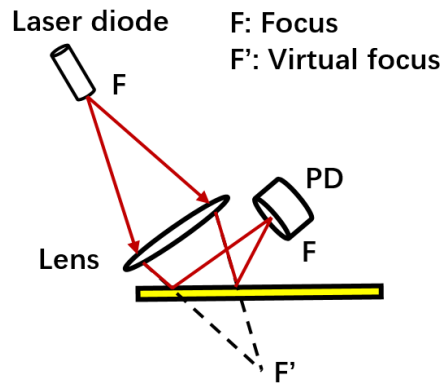
Figure 2.1: The schematic diagram of the optical microphone working principle. Yellow part stands for the movable membrane.

metrically on both sides of the light source, as shown in the Figure 2.2. Due to the divergence angle of the central beam, the reflected light field is radially distributed on the two light sensors. The vertical movement and tilt of the mirror surface will respectively produce the same and opposite changes in the light intensity on both sides [14]. The author has carried out mathematical derivation of this geometry-based measuring methods in detail in the publication, and obtained high-resolution and large measuring range ($0.4mm$ and 2.5 degrees) devices.
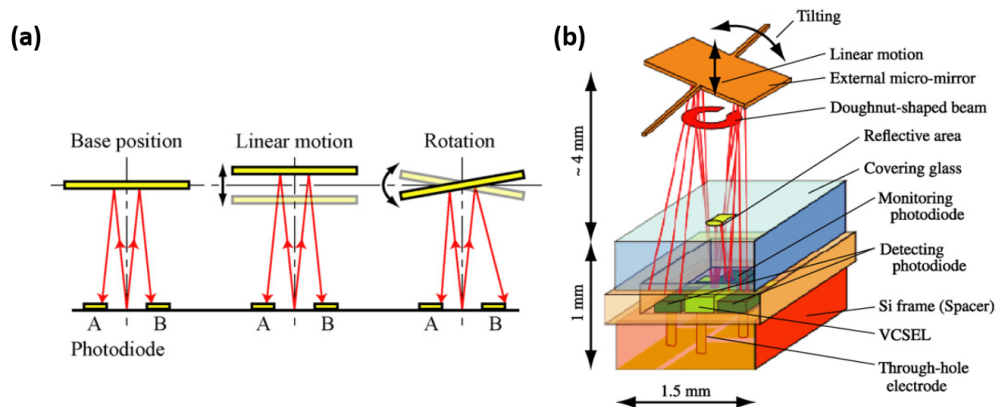
Figure 2.2: Schematic diagram of the effect of vertical displacement and tilt of the reflector on the light field (a) and the testing device (b).

The resolution of the optical detection system depends on the response of changes in the light field distribution to small displacements. Theoretically, this purely reflective structure needs to increase the optical path length to improve the resolution. However, it is limited by device size and processing requirements.

2.2   Grating diffraction

In order to further optimize the resolution of the optical measurement system, a lot of research work focuses on the diffracted light field. The structure shown in the Figure 2.3 is generally adopted, where a the reflection grating is set on the movable structure to be tested.
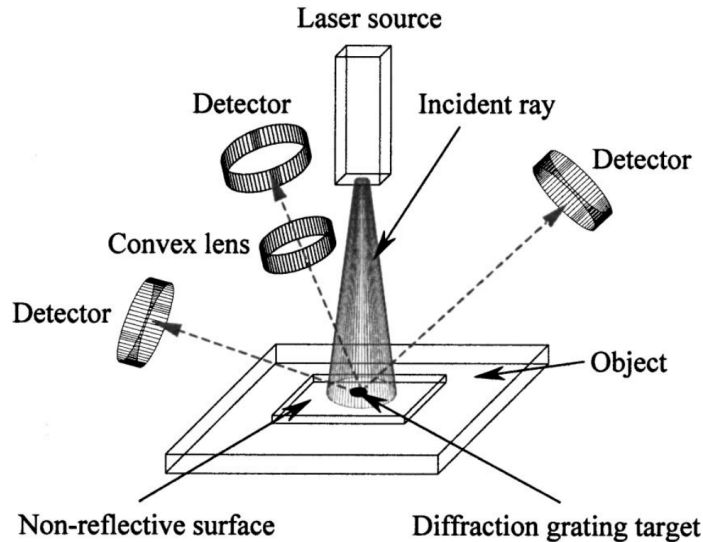
Figure 2.3: Schematic diagram of diffraction optical micro-displacement detection system [15].

The diffractive optical detection system structure is shown in the Figure 2.4. The operating principle includes flowing steps:

(a) The reflected grating with sub-micron width fringes is irradiated by a laser beam. The light passing through the grating gap is absorbed by the underlying material. The light reflected on the grating fringes is diffracted, forming a group of coherent light.

(b) The diffracted light interferes to form a diffraction pattern, which includes diffracted orders with maximum light intensity.

(c) Set the a charge-coupled device (CCD) or PDs array to measure the light intensity of the first diffracted order. According to the multiple slits Fraunhofer diffraction theory [16], the diffraction angle corresponding to each diffracted order is determined by the grating structure and the wavelength of the light source. So the position of the diffracted order (the distance from the center point) is equal to the diffraction angle multiplied by the light transmission distance (working distance), from the grating to the plane where the detector is located.

(d) The working distance is changed, when the diffraction grating moves. So the po-

sition of each diffracted order will shift and be measured. When the grating moves in the vertical direction, the positive and negative diffracted orders move in opposite directions. When the grating rotates or tilts, the positive and negative diffracted orders move in the same direction. Through geometric calculation, the displacement of the diffraction grating can be calculated using the moving distance of the diffracted orders.
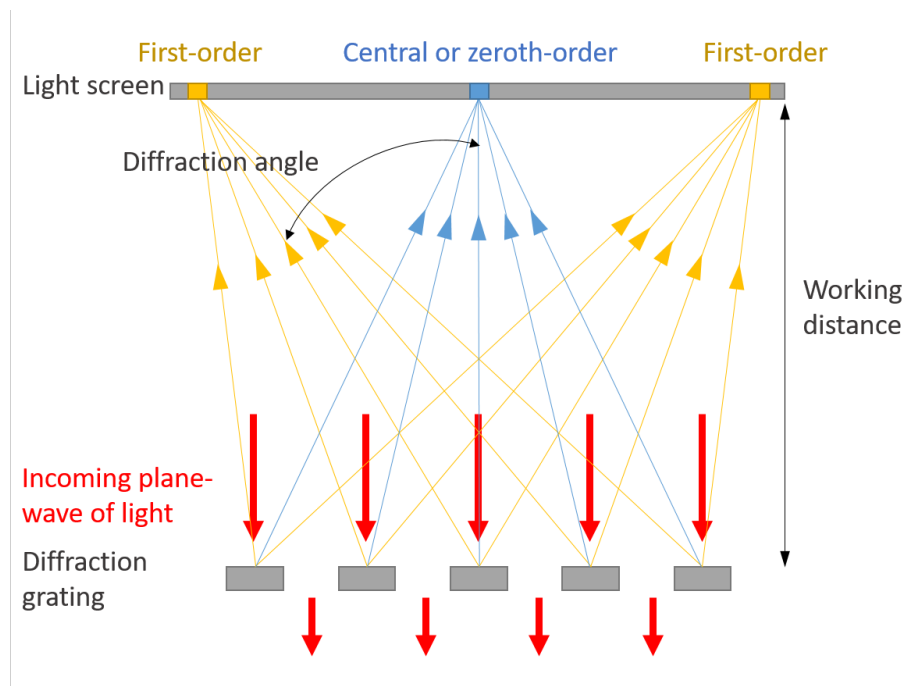
Figure 2.4: Schematic diagram of grating diffraction.

Compared with the detection of the overall intensity of the light field in a purely reflective system, the effective light intensity signal is concentrated in each diffracted order. So the change in the position of the diffracted order is easier to be measured. Therefore, the accuracy of this type of measurement system can usually be very sensitive to changes in tilt angle in micron-degree scale [17]–[19].

2.3   Double grating diffraction

Double grating interference detection has been successfully applied in displacement and acceleration detection [20]–[22]. Through structural design, two sets of diffraction gratings that interfere with each other and the compound light field can be obtained. Based on the vector diffraction theory, it can convert weak displacement changes into regular fluctuations of light intensity. The accuracy of interferometry

can reach picometer level or even higher, and the structure is simpler and more reliable. Also the complementary outputs derived from zeroth and higher diffracted orders reduce the effect of laser intensity noise in the measurements [12], [23].

The basic operating principle is to add a reflective surface (fixed on the movable structure) behind the reflective grating, and the reflected light beam passes through the grating again to form a transmissive grating. The two sets of light fields interfere with each other to form the final diffraction pattern. Similar to the diffraction detection system, the detectors only measures the intensity of certain diffracted orders. When the reflecting surface moves, the initial phase of the transmitted diffracted light field changes due to the change of the optical path. Eventually it will affect the intensity of the composite diffracted orders. The detailed principle explanation is introduced in Chapter 3. Due to the periodicity of the light phase, the resolution of this detection method can reach the order of nanometers.

Since 2000, Neal A. Hall's team form Georgia Institute of Technology, has applied integrated optical interference detection methods to micromechanical capacitive acoustic sensors [24], [25], as shown in the Figure 2.5(a). The incident light beam is reflected by the metal electrode grating and the upper vibration film. By measuring the intensity of the diffracted orders, the displacement of the moving film can be determined. By adjusting the voltage of the grating structure and the metal film, the dynamic response of the device can be adjusted through force feedback to keep the sensitivity at the optimal level. The device reported in 2002 can achieve a minimum detectable displacement of 2×10^{-4} Å$/\sqrt{Hz}$ around $250kHz$ and low frequency detection capability for microphone applications [26].

In 2004, the same group integrated a detector array and an optical sensor chip. This structure achieves a good integration while ensuring excellent displacement resolution, reaching $20fm/\sqrt{Hz}$ at $20kHz$ [27], shown in the Figure 2.5(b).

From 2004 to 2008, B. Kim's team replaced the mirror part of the double grating structure with the detection object, and successfully realized the micro-scanning grating interferometer [28]–[30]. After the sensitive units are arranged in an array, they can be used to test the surface undulating motion of other objects. The structure and detection diagram are shown in Figure 2.6.

Due to the periodicity of the light field propagation, the light intensity changes with the displacement in the grating interference detection in a sinusoidal form, the light intensity changes little at the peak and trough, and the highest sensitivity is achieved in the middle of the range [31]. So the displacement detection range and sensitivity are limited. In order to expand the test range, in 2007, researchers at Georgia Institute of Technology reported an integrated double grating difference measurement method for atomic force microscope probes [32], as shown in Figure 2.7. The phase
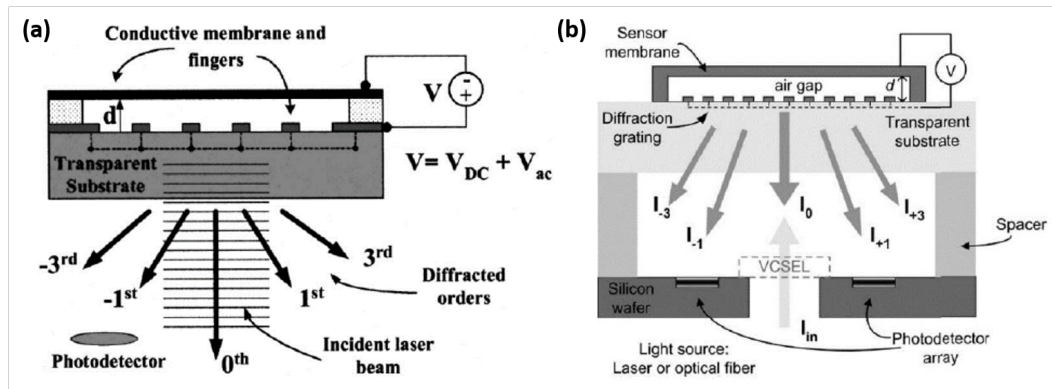
Figure 2.5: (a) Schematic diagram of sound sensor structure based on double grating structure [26],(b) Schematic diagram of the sensor structure of the integrated silicon photoelectric detection chip array [27].
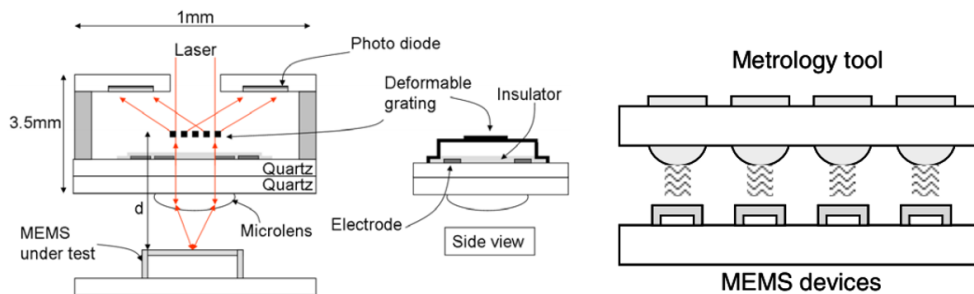

Figure 2.6: Schematic diagram of array type grating interference device [28].

is adjusted through the propagation medium, and the left and right photodetectors respectively receive effective signals with a 90 degrees phase difference. Since the response of the optical signal to the displacement of the mirror is a sinusoidal curve, when one optical signal is in the region of poor linearity, the other optical signal with a phase difference of 90 degrees is in the region of good linearity. Also, the region with better linearity corresponds to higher sensitivity (slope). By combining the linear regions of the two sets of signals, it can be ensured that the displacement response is always maintained in the region of greater sensitivity. In 2009, the same research group also used the electrostatic force feedback method to optimize the high sensitivity [33], as shown in Figure 2.8. The position of the grating is adjusted according to the feedback of the detection result (the step length is $4/\lambda$) to ensure that the small displacement to be detected is always kept in the most sensitive ranges. The Feng's research group of Tsinghua University applied this structure to liquid biochemical detection, in 2013 [34]. Analyzed in principle, these two methods are designed to change the initial phase difference of the two sets of diffraction grating light fields. Compared with the first method, the adjustable grating method has a more flexible

and wider adjustment range. Simultaneously, it can also avoid the strict require-
ments of the optical medium etching process, including the depth accuracy and the
flatness of the etching surface (excessive roughness will cause too much light dif-
fuse reflection and weaken the light intensity). For the second method, the complex
feedback control algorithm is the key factor, such as a look-up table is used to map
the controller output to a nonlinear curve. In related publications, the authors gave
a more detailed introduction.
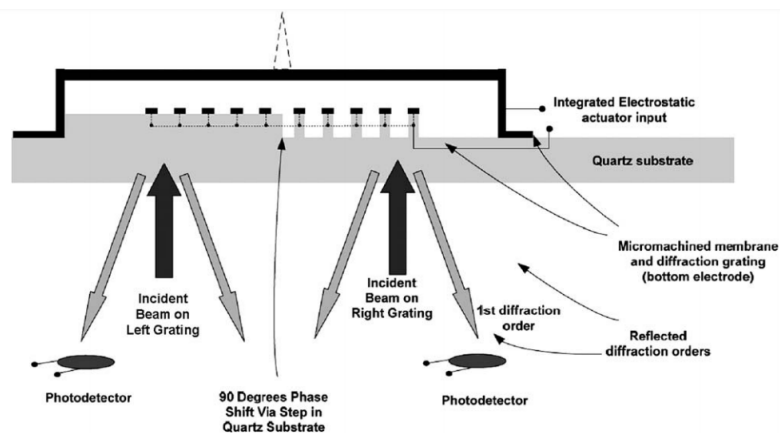
Figure 2.7: Schematic diagram of double grating detection structure with initial
phase difference [31].
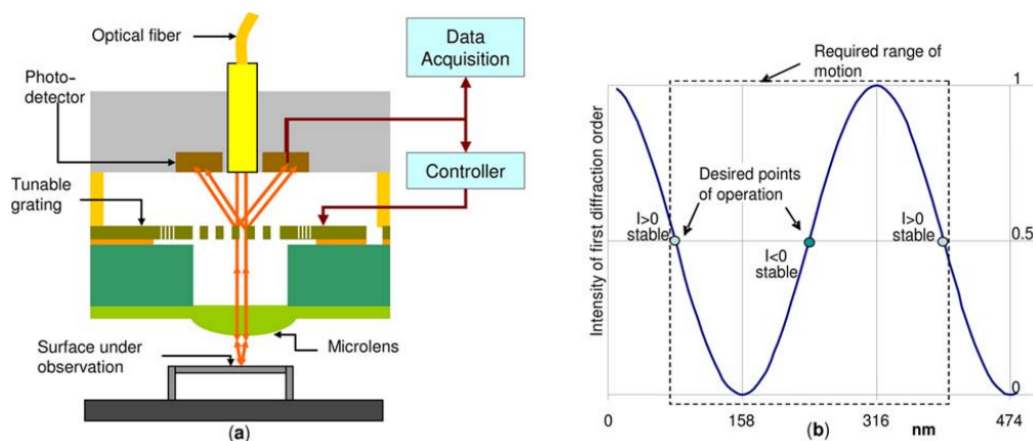
Figure 2.8: (a) Schematic diagram of tunable grating microinterferometer and its
control [33]. (b) Normalized optical intensity curve for the first diffracted
order [33].

Researchers from Koc University have reported a detection system with adjustable
wavelength [31], as shown in the Figure 2.9. The light sources can alternately excite

light beams of different wavelengths, and the light-sensitive elements are respectively arranged corresponding to different diffraction angles to obtain interference signals. In this setup, the grating is alternately illuminated by different light sources in chronological order, and different high sensitivity ranges will be obtained. The calibration routine is used to evaluate the high sensitivity range of different wavelengths, and only the signal corresponding to the wavelength that matches the displacement amplitude is selected in the measurement process. Therefore, the detection sensitivity will be enhanced, which theoretically conforms to: $S_{2\lambda} = \max\{S_{\lambda_1}, S_{\lambda_2}\}$. As they published in 2007, 2010 and 2011, the sensitivity of the sensor array is increased by 30 percents on average [31], [35], [36]. And in theory, it can continue to be improved by rationally designing the optical path and more light sources.
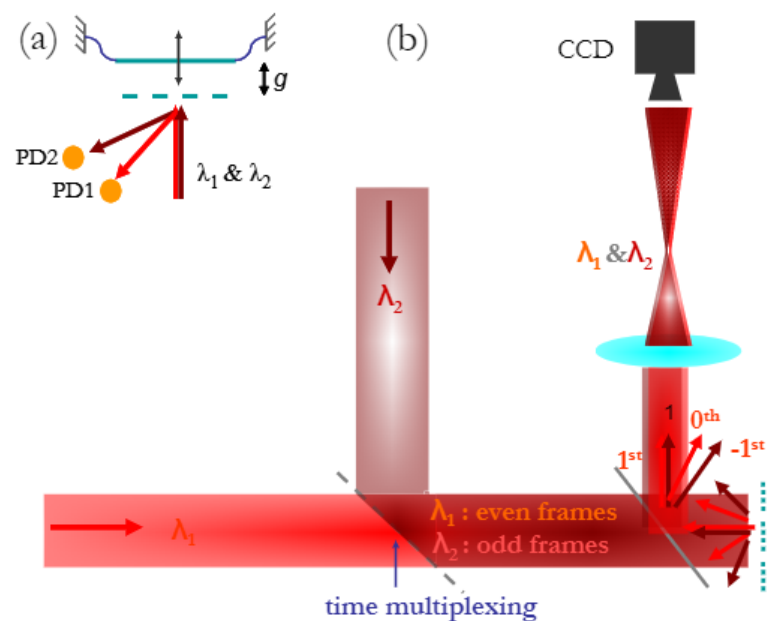
Figure 2.9: (a) Diffraction grating based MEMS Sensor that is illuminated with two lasers with two wavelengths. (b) Proposed method using two – wavelength illumination where the sensor array is illuminated by two sources, one at a time. The first diffracted order light is imaged onto an array of photodetectors, i.e a CCD camera [31].

In 2009, the Kang Wu group of Tsinghua University reported a grating accelerometer. The influence of the deflection of the simulated mirror on the detection light intensity is calculated by the scalar diffraction theory, and the structure is shown in Figure 2.10. The device structure adopts anodic bonding process, and the spacing is adjusted by electrostatic attraction. The displacement amplitude of the sensing structure of the device is $159nm$, and the measurement resolution is about

$0.2nm$ [37].
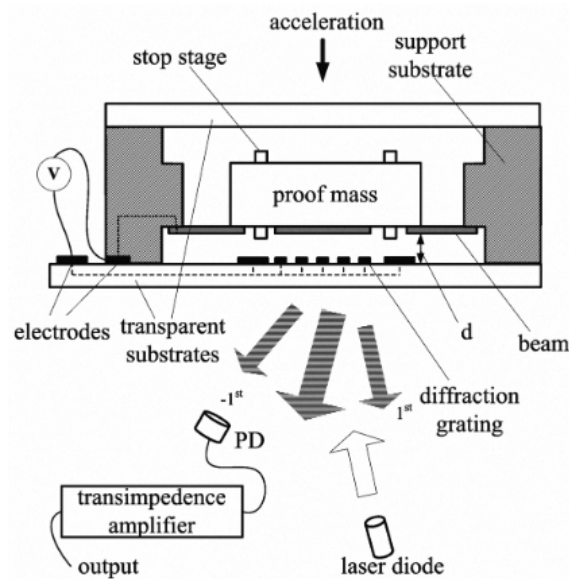
**Figure 2.10:** Schematic of the interferometric accelerometer [37].

Beijing University of Aeronautics and Astronautics proposed an improved optical sensor structure based on micron double grating in 2010 [38], as shown in Figure 2.11. Corresponding to the bottom of the diffraction grating, a metal layer is made as a mirror, and the light beam forms interference between the diffraction grating mirrors to achieve the purpose of improving measurement accuracy. Researchers conduct theoretical analysis and derivation of mathematical models for sensor principles. Subsequent actual processing and testing show that the reflectivity of the mirror has a greater impact on the optical measurement sensitivity. In a report published in 2019, this team demonstrated the application of this structure to the measurement of small displacements in inertial navigation devices [39], [40]. The acceleration measurement with a scale factor improvement, noise floor decrease, and thus a bias stability enhancement from $2mg$ to $0.35mg$, which was achieved by reducing the non-parallelism error.

Zhejiang University proposed an optical tilt sensor based on a modulated phase-sensitive diffraction grating in 2011 [41]. As shown in Figure 2.12(a), the mechanical sensing part includes a mass and two supporting cantilever structures, which can be fabricated on a silicon substrate using a dual mask process. The integrated photosensitive element can detect the changes in the diffraction spectrum caused by the tilt of the mirror. The experimental results show that the best inclination sensitivity of the sensor is $1.15V/degree$, the resolution is about 0.0046 degrees, and the measurement range perpendicular to the gravity direction of the earth is $0-20$ degrees.
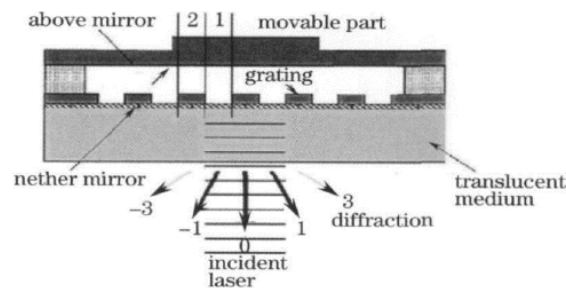
Figure 2.11: Schematic of the interferometric accelerometer [39].

In 2015, the same research group reported a grating sensor based on light intensity compensation and phase modulation [42]. As shown in Figure 2.12(b), the compensation optical path and piezoelectric ceramic driver have been added to the previous detection. Phase modulation technology can improve the signal-to-noise ratio, so the signal stability is greatly improved. Experimental results show that the sensitivity of the grating displacement sensor is $44.75mV/nm$, and the highest resolution can reach $0.017nm$, which is 27 times that of the sensor without intensity compensation and phase modulation.
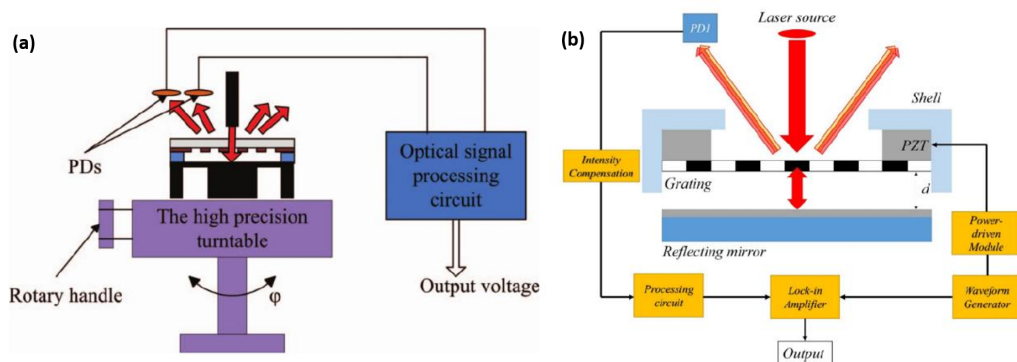
Figure 2.12: (a)Schematic of the grating type tilt sensor [41], (b)Schematic of the phase modulation type grating displacement sensor [42].

In 2019, Bauman State Technical University Odinokov group theoretically proved a interference linear displacement sensor based on phase shifts measurement of light in orders of diffraction grating [43].The structure of the model is shown in the Figure 2.13. Two sets of code rulers form a double grating structure, and the diffraction intensity distribution map is obtained through the optical sensor. The diffracted order profile based on numerical simulation will cause phase changes due to the moving code rule, which helps reaching the required measurement accuracy with nanometric resolution.
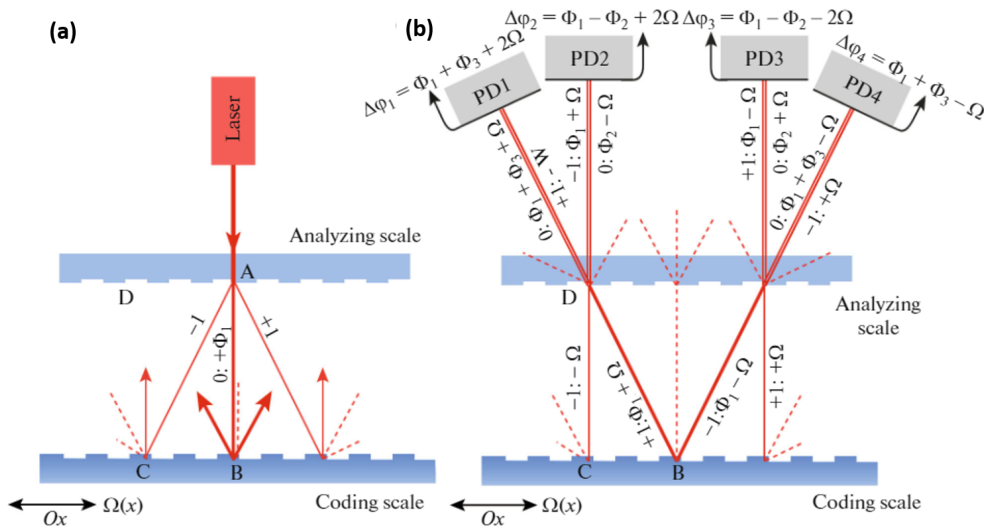
Figure 2.13: Light path in the optical scheme [43]: (a) when the radiation propagates from the source to the coding scale and (b) when it prop-agates after diffraction at the coding scale.

Because of its simple test structure and high sensitivity, the double grating interferometry has moved from the early theory to sensor applications, and has been researched and applied in gravimeters, microphones, displacement sensors, accelerometers, and biochemical detection. Simultaneously, the sensitivity and dynamic response can also be improved by assembling this micro-system with the existing optical sensor. For example, Yu Zhang group combined the double-grating structure with the existing laser accelerometer to enhance the bias stability from $2mg$ to $0.35mg$ by reducing the non-parallelism error [39], as shown in Figure 2.14. With the development of optoelectronic devices with the gradual miniaturization, the integration of optical detection into micro-inertial devices has great potential for development.
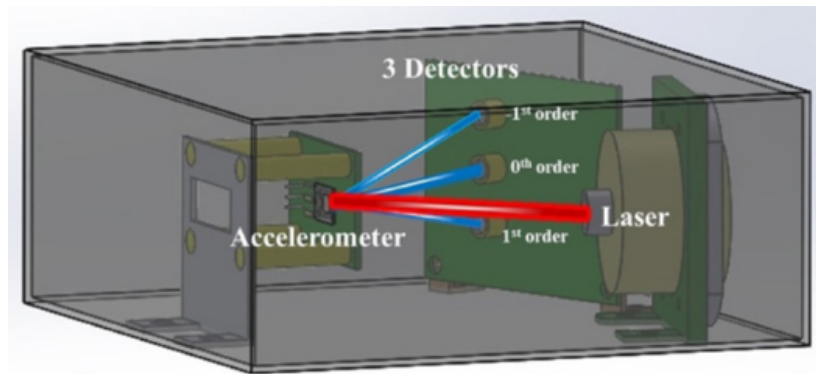
Figure 2.14: Schematic diagram of an optical accelerometer [39]. A glass cover
with a metal deposition grating is added above the accelerometer to
form a double grating structure.

Working Principle

According to the structure of the Coriolis flow sensor in this project, we use a double grating structure to achieve optical readout. As shown in the Figure 3.1, the central part of the suspended micro-tube where gold is deposited in the original structure is used as a reflecting mirror. A metal grating, a light source and a light sensor array are set above it (the specific layout is described in Chapter 4). In this way, the displacement of the suspended micro-tube will cause the change of the diffracted light field. By recording the change of the light intensity signal by the PDs, the movement of the micro-tube can be detected. Such a design can not only take advantage of the high sensitivity of diffractive optical detection, but also facilitate the layout of light sources and sensor components, without affecting the existing sensor structure.
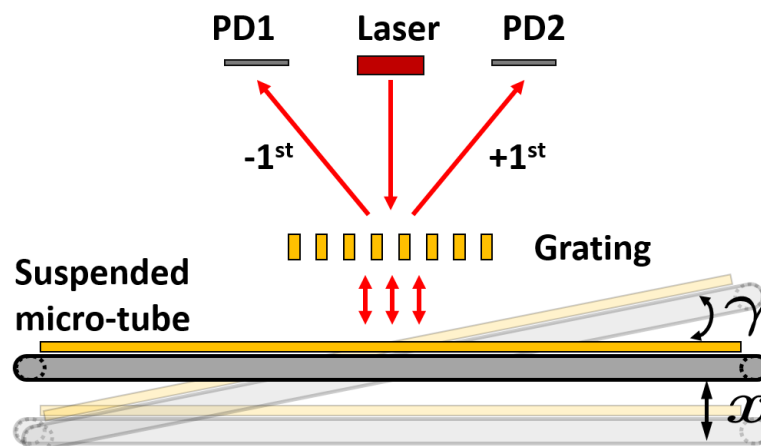
Figure 3.1: The schematic of the double grating structure set above the Coriolis flow sensor.

The schematic of the double grating system is presented in Figure 3.2. The gold-deposited grating surface has good reflectivity, with a grating period of d and a grating slit width of a. The initial distance between the reflector and the grating is h.
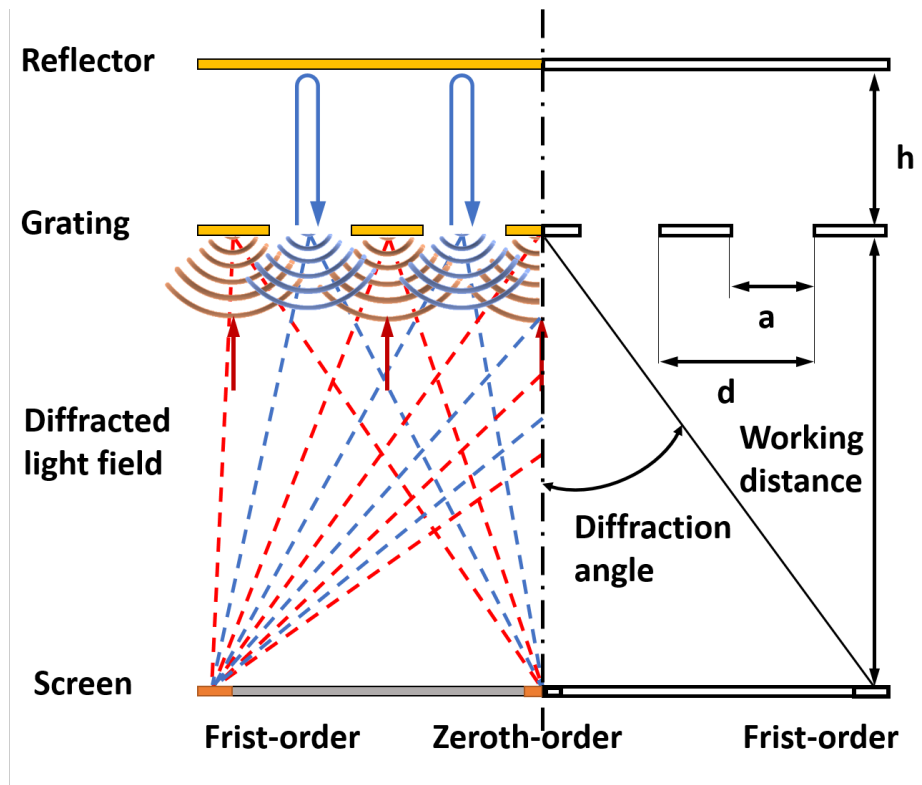
Figure 3.2: The schematic of the double grating structure. The plane wave is incident perpendicularly from below and is reflected by the grating (red arrows). The light transmitted through the slits is reflected by the reflector and then emitted from the slits again (blue arrows). The red-marked and blue-marked diffracted field respectively represent the reflection diffraction grating and the transmission diffraction grating. The two sets of diffraction light fields (red and blue dot-lines) interfere to form a composite diffracted orders.

The operating principle includes the flowing steps:

(a) The light source generates a incident plane wave in the radial direction to illuminate the fixed reflective grating. Since the grating slit width is close to the wavelength of the source, a significant diffraction effect occurs. The light reflected by the metal fingers has the same phase as the first group of diffracted field, starting from the surface of the grating. This group of light sources interfere with each other to produce a diffraction pattern, and the diffracted orders with significantly enhanced light intensity appears at specific diffraction angles.

Following the principle of multiple slits Fraunhofer diffraction [16], [44], the total electric field from N fingers in a grating is the sum of individual contributions. So the electric field of the first grating can be expressed as:

$$E_1 = A \left[\frac{\sin(\alpha_1)}{\alpha_1} \right] \cdot \left[\exp\left[i\left(-\frac{N-1}{2} \right) \delta_1 \right] + \exp\left[i\left(-\frac{N-1}{2} + 1 \right) \delta_1 \right] \right.$$
$$\left. + \cdots + 1 + \cdots + \exp\left[i\left(\frac{N-1}{2} \right) \right] \delta_1 \right] \tag{3.1}$$
$$= A \left[\frac{\sin(\alpha_1)}{\alpha_1} \right] \cdot \left[\frac{\sin\left(\frac{N}{2}\delta_1 \right)}{\sin\left(\frac{\delta_1}{2} \right)} \right] \cdot \exp[i\delta_1]$$

Where A is the amplitude of the light field as a constant. The diffraction factor is $\alpha_1 = \frac{\pi}{\lambda}(d-a)\sin\theta$. The $(d-a)$ is the width of the metal strips of the grating, which mainly determining the distribution of luminous fluxes of the reflection grating and transmission grating. θ is the diffraction angle and λ is the light source's wavelength. The light path difference of two adjacent diffracted fields is $\delta_1 = \frac{2\pi}{\lambda}d\sin\theta$. Since the structure is symmetrical in the center, the central diffracted field is used as a reference. So that the diffracted fields on both sides increase and decrease the optical path respectively, corresponding to the complex exponential terms in the expression. N is the number of metal strips covered by the incident light beam and determines the quality of the diffraction pattern. The more grating strips, the more obvious the light-dark boundary of the diffracted orders. The simplification process of this formula and the following light field expression is shown in the Appendix A.

(b) The light transmitted through the slits of the reflective grating is irradiated on the movable reflector surface. In the structure of the flow sensor, the reflector is the gold deposited metal plane on suspended micro-tube, in the middle of the y-axis parallel segment. The reflected light will re-enter the grating plane. At this time, the light passing through the grating slit forms a second group of diffracted field due to the diffraction effect. The transmission grating will still form a diffraction pattern under the interference of the diffracted fields. The electric field of incident light which passes the transmission grating is expressed as:

$$E_2 = A \left[\frac{\sin(\alpha_2)}{\alpha_2} \right] \cdot \left[\frac{\sin\left(\frac{N}{2}\delta_2 \right)}{\sin\left(\frac{\delta_2}{2} \right)} \right] \cdot \exp[i\delta_2] \cdot \exp[i(\delta_i + 2kh)] \tag{3.2}$$

Since the slits, with width of a, are the diffracted field position of the transmission grating, the diffraction factor is $\alpha_2 = \frac{\pi}{\lambda}a\sin\theta$. The optical path difference between adjacent slits is $\delta_2 = \frac{2\pi}{\lambda}d\sin\theta$, which is also determined by the grating period like δ_1. The small position difference between each of the metal stripes and slits needs to be considered and corresponds as $\delta_i = \frac{\pi}{\lambda}(d-a)\sin\theta$. Since the reflector is parallel to the grating, the initial phase difference of the diffracted fields caused by the reflection process is equal, as $\exp(i2kh)$, where k is the wave number, equaling to $1/\lambda$.

(c) The two diffracted light fields interfere with each other. In the numerical calcula-
tion, it is the superposition of electric field intensity. So the intensities of diffracted
field can be given as:

$$I = |E_1 + E_2|^2 \tag{3.3}$$

(d) The reflection of light between the grating and the reflector causes an additional
optical path, equal to twice the gap distance. The optical path difference of the two
sets of diffracted fields leads to the initial phase difference, which in turn affects
the composite diffraction effect. Therefore, when the reflector moves, the optical
path difference of the two sets of light sources will correspondingly change, which
eventually leads to a change in the intensity distribution of the diffracted light field.
The light detector is set at the position corresponding to the detected diffracted order,
so that the movement of the reflector can be reflected by accurately measuring the
change in light intensity.
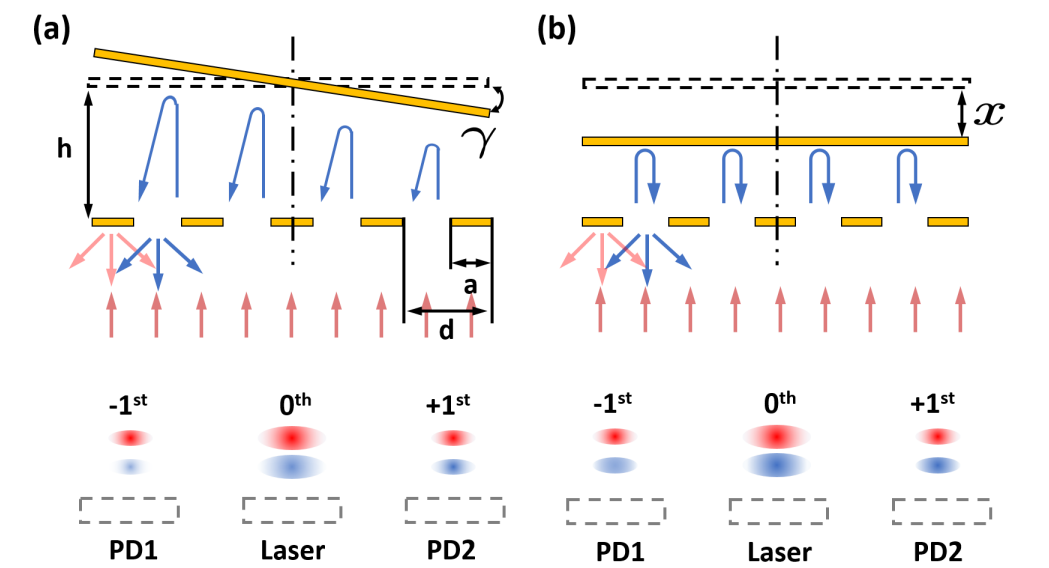
Figure 3.3: The schematic of the center rotational (a) and vertical (b) displacement
of the reflector in the double grating structure. The red spots and the
blue spots respectively indicate the diffracted orders of the reflection
grating and the transmission grating. In reality, since the grating coef-
ficients are the same, the positions of the two sets of diffracted orders
are the same. The light field interference determines the light intensity
of each diffracted order.

In addition, the reflector has two different motion modes, translational motion and
rotation, as shown in Figure 3.3. Each movement has a different effect on the optical

path difference, cause the electric field of the transmission grating to be adjusted as:

$$E_2 = A \left[\frac{\sin(\alpha_2)}{\alpha_2}\right] \cdot \exp[i\delta_i] \cdot \exp[i2k(h+x)] \cdot \left[\frac{\sin\left(\frac{N}{2}\varphi\right)}{\sin\left(\frac{\varphi}{2}\right)}\right] \cdot \exp[i\varphi] \tag{3.4}$$

Where diffracted actor is $\alpha_2 = \frac{\pi}{\lambda} \cdot a \cdot (\sin\theta - \sin\gamma)$. Stripe-slit optical path difference is $\alpha_i = \frac{\pi}{\lambda}(d-a)\sin\theta$. Reflector-grating gap caused phase difference is $\exp[i2k(h+x)]$, where x is the vertical displacement of the reflector. Most importantly, the slit-slit optical path difference changes due to the tilt angle, $\varphi = \delta_2 + 2kd\sin\gamma$, where $\delta_2 = \frac{\pi}{\lambda} \cdot d \cdot (\sin\theta - \sin\gamma)$.

The electric field and light intensity distribution of the superposition of the two diffractions still follow Equation (3.3).

The effect of translational motion is easier to analyse. When the reflector is getting closer to the grating, the phase of the diffracted field of the transmission grating is reduced synchronously. So the result of superposition with the diffracted light field of the reflection grating is changed. It is similar to the effect of a group of sine waves with reduced phase superimposed on another group of sine waves with a fixed phase. According to the periodicity of wave optics, when the translation distance is an integer multiple of half a wavelength, the superimposed light field changes periodically.

When the reflector rotates along the center of symmetry, due to the angle between the reflector and the fixed grating plane, the light diffracted from the grating slits will have different optical path differences. The initial phase difference of the diffracted field of the transmission grating will cause two changes in the light field distribution on the monitoring plane parallel to the grating:

First, the intensity of the diffraction pattern will change and will no longer be symmetrical along the center.

Secondly, the diffraction angle corresponding to the diffracted orders will change. This means that the distribution positions of each diffracted orders on the monitoring plane will change, which will cause misalignment with the fixed reflection grating pattern.

It can be seen from equation (3.3) of the diffraction electric field that the influence of the two movements of the reflector on the field strength determines the sensitivity of this optical reading system.

(e) Quantitatively measurement of these two motions can be achieved by comparing the phase difference between the light intensity changes of the positive and negative first diffracted orders.

The reflector rotates periodically in the initial drive mode. Due to geometric symmetry, the light intensity of the positive and negative first diffracted orders will change oppositely, so the initial phase difference between the two optical signals is pi.

When the Coriolis force causes the mirror to move vertically, the phase of the light field of the transmission grating changes equally. Therefore, the optical signals of the positive and negative first-order diffracted orders will all change synchronously, determined by the amplitude of the vertical movement.

This effect will be reflected in the change in the phase of the optical signal. This phase shift test method is numerically calculated in the next chapter, and the sensitivity is analyzed.

Theoretical verification

In this chapter, according to the working principle, the double grating diffraction based optical readout system is designed. Numerical calculations and optical simulations are carried out according to the geometric parameters of the design, which verified the feasibility. And the sensitivity of the system is evaluated by the measurement method of phase shift.

4.1 Optical readout system design

The project intends to use VCSEL as the light source with a wavelength of $850nm$. The VCSEL package size is small and high beam quality. Also, unlike the edge-emitting laser (EEL), the VCSEL laser is emitting from the top surface. Therefore, as a surface mount component (SMD), it is more convenient for structure design, which will be reflected in the subsequent photomask design. The structural parameters of alternative VCSEL and PDs devices are given in the Figure 4.1.
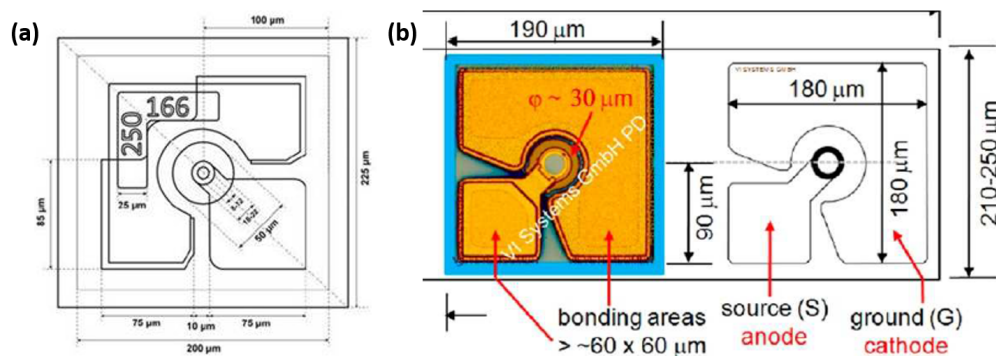
Figure 4.1: The size parameters of VCSEL and PDs devices.

As shown in Figure 4.2 (a), without changing the original layout of the micro Coriolis

flow sensor, the entire optical readout system will be integrated on a glass substrate, which has good transparency to $850nm$ light. The patterned gold layers are deposited on both sides of the glass wafer to serve as the grating structure and electrical interface for the devices. The light source and the light detector can be bonded to the glass substrate by flip-chip bonding method. So the incident light directly enters the glass and diffraction and interference occur in the same medium. This design minimizes the refraction phenomenon that occurs at the glass-air interfaces to ensure that the positions of the each diffracted orders are the same as expected. Summarizing the size design of the structure in the literature, the strip grating with a width of $4um$ meets the diffraction requirements of common laser diodes ($600 - 900nm$ wavelength) and has low manufacturing process requirements. So in this project, the same grating period was selected. The initial distance between the grating and the reflector is controlled by the thickness of the spacer. On the premise of ensuring that the moving reflector will not collide with the fixed structure, the thinner spacer reduces the light dissipation. In principle, this initial distance does not affect the position of the diffraction order.

The working distance, the distance between the grating and the detector, is determined by the thickness of the glass substrate. By calculating the diffraction angle based on the grating formula, Equation (4.1), for a grating period of $4um$, the position of the first diffracted order is about $212.5um$ from the center point, at a working distance of $1mm$. Therefore, to arrange the selected light source and detectors with sufficient space, the thickness of the glass substrate should not be less than $1mm$.

$$d \sin \theta = m\lambda, m = 0, \pm 1, \pm 2, \pm 3 \cdots \tag{4.1}$$

Based on the devices parameters and layout, the photomask of the optical readout system is drawn, as shown in Figure 4.2(b).

4.2 Numerical Calculation for Sensitivity of the System

The micro-tube in the micro Coriolis mass flow sensor has a periodic rotation or twist mode driven by the initial Lorentz force. When the fluid passes through, the periodic swing mode or vertical movement caused by the Coriolis force will be superimposed. Corresponding to the optical detection system, the light intensity of the first diffracted order is detected by the PDs, and the initial rotating motion will produce a periodically light signal. The periodic signal caused by the vertical movement will have the
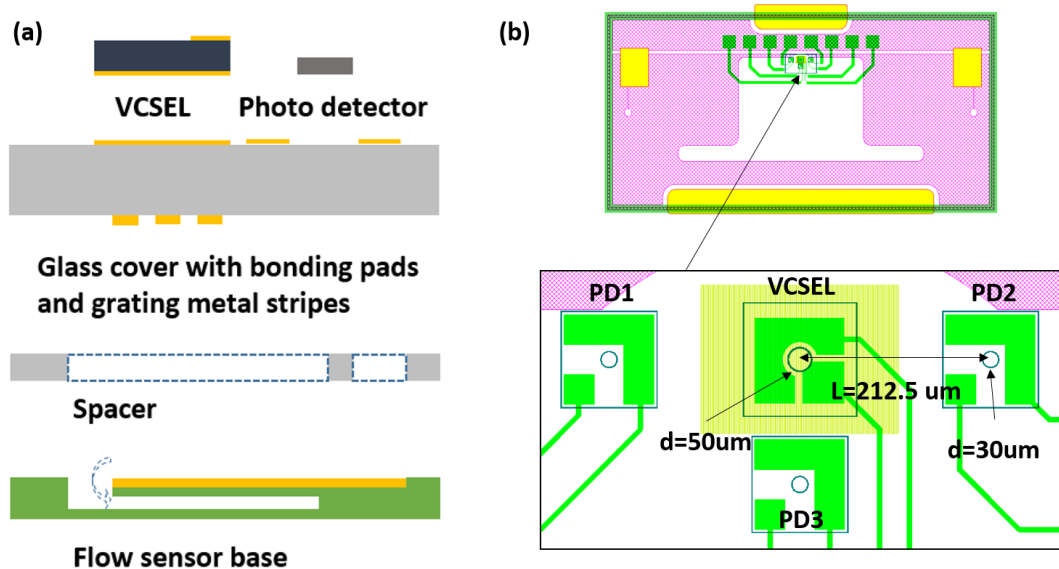
Figure 4.2: (a) Multi-layer stacking for optical readout system. Top-layer is the glass cover and also the carrier of the light source, PDs, and deposited metal grating (yellow parts). Mid-layer is the insulated layer as spacer with through holes for electrical connection of the flow sensor. Bottom-layer is the originally designed chip of the micro Coriolis mass flow sensor. The cantilever beam in the figure represents the side view of the suspended micro-tube loop which deposited reflective metal layer on the top surface (yellow part). The micro-tube can move in a sealed cavity composed of the bottom etched area and the upper two layers. (b) Glass cover photomask design. Yellow: Glass cavity. Pink: Glass bonding. Green: Metal layer. Light yellow: Metal layer(back side). PD1 and PD2 measure the intensity of the first diffracted order. PD3 is used as a reference to reduce the noise.

same frequency and an initial phase difference of 90 degrees. Superimposing the periodic vertical motion signal on the original periodic signal will cause a phase shift. The magnitude of this phase shift can reflect the peak value of the vertical motion signal and deduce the corresponding physical displacement of the reflector.

Figure 4.3 illustrates the mathematically calculated profiles of diffraction electric field, based on the expressions of double grating model, Equation (3.2) - (3.4). The structural parameters are listed in the following Table 4.1. The distance from grating to reflector is controlled in the micron order by depositing an spacer layer. The distance from grating to photodetector corresponds to the design of the mask and is set to $1000um$. Comparing the diffraction results of diffraction grating and transmission grating respectively (a and b) and the interference result (c), we can find the position of each diffracted orders based on the calculation of the grating formula, Equation (4.1).

Table 4.1: The parameters of the double grating structure model for calculation

Parameter	Value
Wavelength of light source (λ)	$850nm$
Grating period (d)	$4um$
Grating slit width (a)	$2um$
Distance from grating to reflector (h)	$8um$
Distance from grating to photodetector (L)	$1000um$
Light beam width (W)	$400um$
Light amplitude constant (A)	1

The grating periods corresponding to the two sets of diffraction are the same, so the diffraction angles are the same. In addition, since the grating ratio (a/d) is 0.5, the total light intensity of the two sets of gratings is equal. Therefore, the two sets of diffraction patterns have consistency. Also, due to the superposition of light fields, the light intensity of each diffracted orders of the interference result changes. The light intensities of the first diffracted order before and after the interference are 4053 and 4493, respectively. The numerical value shows that this superposition of light field is not a numerical addition. According to vector addition calculation as Equation (4.2) - (4.3), the phase angle difference of two set of light is $2.03rad$, which is consistent with the calculated design results of the optical path difference and satisfied with the description of interference in optical wave theory.
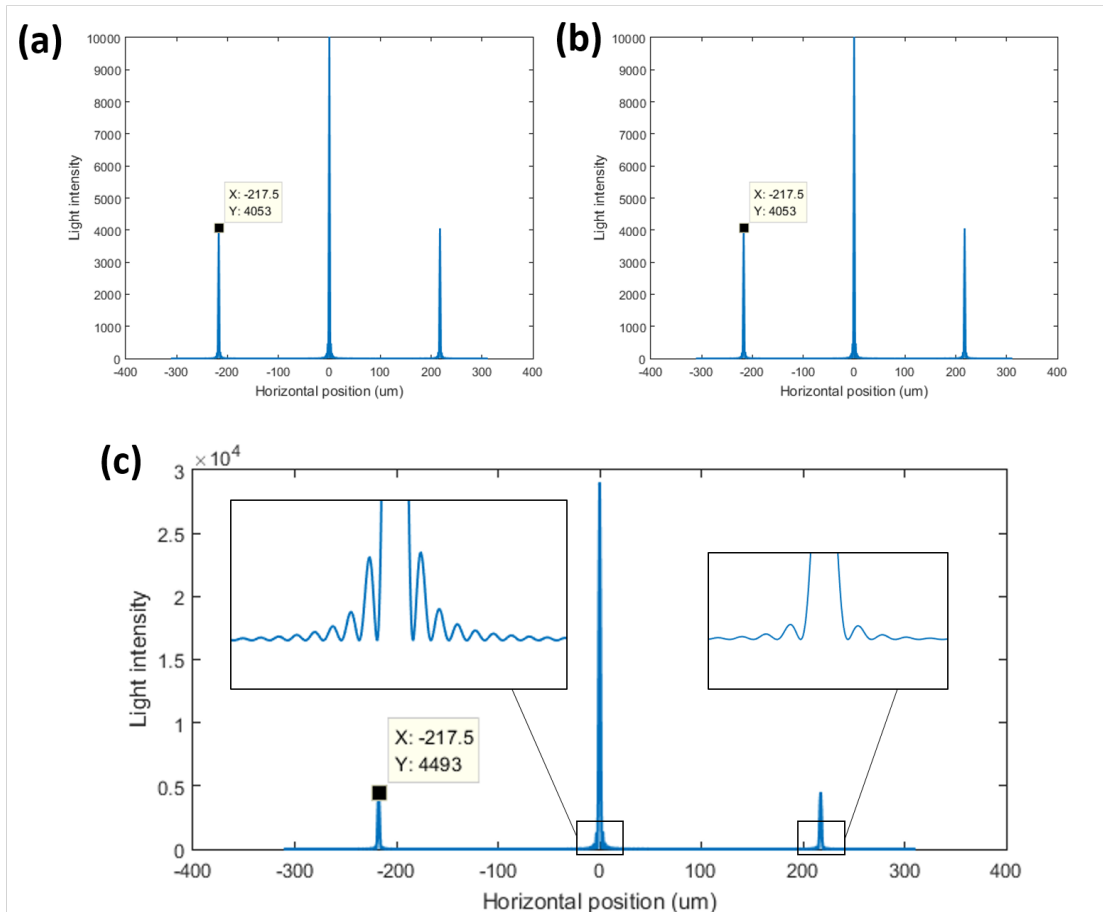
Figure 4.3: The calculation results of the light intensity of the zero diffracted order and positive and negative first-order diffracted orders (a) Diffraction result of reflection grating. (b) The diffraction result of the transmission grating. (c) The composite diffraction result of the double grating.

$$E_1 = E_2 = \sqrt{4053} = 661.63.66, E = \sqrt{4493} = 67.03$$

$$Numerical : \Delta\varphi = \varphi_2 - \varphi_1 = \arccos\left[\frac{E^2 - E_1^2 - E_2^2}{2E_1 E_2}\right] = 2.03 rad \qquad (4.2)$$

$$Geometrical : \Delta\varphi = 2\pi/\lambda \times MOD\left(\frac{2h}{\lambda}\right) - \delta_i = 2.03 rad \qquad (4.3)$$

where, the δ_i is the optical path difference caused by the grating fringe width. In addition, reflection will cause the phase of the light to reverse (change π), which is equivalent to a half-wavelength reduction in the geometric optical path. There is once reflection in the two diffracted light paths, which occur on the grating surface and the reflector surface respectively. Therefore, the effects of reflections can be offset when calculating the optical path difference.

Changing the distance between the reflector and the grating, the phase difference between the two groups of diffracted fields will change, and eventually lead to a change in the composite diffraction pattern, as shown in the Figure 4.4. Obviously, the vertical movement of the mirror will produce a more obvious periodic signal, by detecting the light intensity of the first diffracted order. The vertical displacement range of the Coriolis flow sensor is approximately $\pm 20 nm$. In this range, the change of light intensity conforms to a sine function, with good resolution. Obviously, the sensitivity is lower near the peak area. Adjusting the initial gap distance to a position with greater sensitivity requires a nanometer-level structural accuracy. Also, the sensitivity can be further increased by increasing the incident light power or the amplifier in the peripheral circuit. For this calculation case, when the gap distance is $0 um$, which means the double grating structure is a perfect reflective surface, the light intensity of the first diffracted order should be 0. Comparing the result in the Figure 4.4(j), the theoretical absolute error is $0.005 um$, which can be changed by adjusting the structural parameters.

By changing the tilt angle of the reflector, for the transmission grating, the light diffracted from different slits has different optical paths, so the initial phases are different. The light field distribution of the transmission grating and the result of interference with the fixed reflection grating will change, as shown in the Figure 4.5. Consistent with the analysis in the previous chapter, when the reflector tilts, the light intensity, diffraction angle and symmetry of the diffracted orders of the transmission grating change accordingly. When the tilt angle is in a certain range, the total light intensity of the composite light field diffracted order remains basically unchanged. At this time, the light intensity will not be able to reflect the change of the angle, forming a 'blind zone'. By increasing the measurement range of the diffraction spot (determined by the size of the photosensitive area of the PD), the range of the "blind zone"
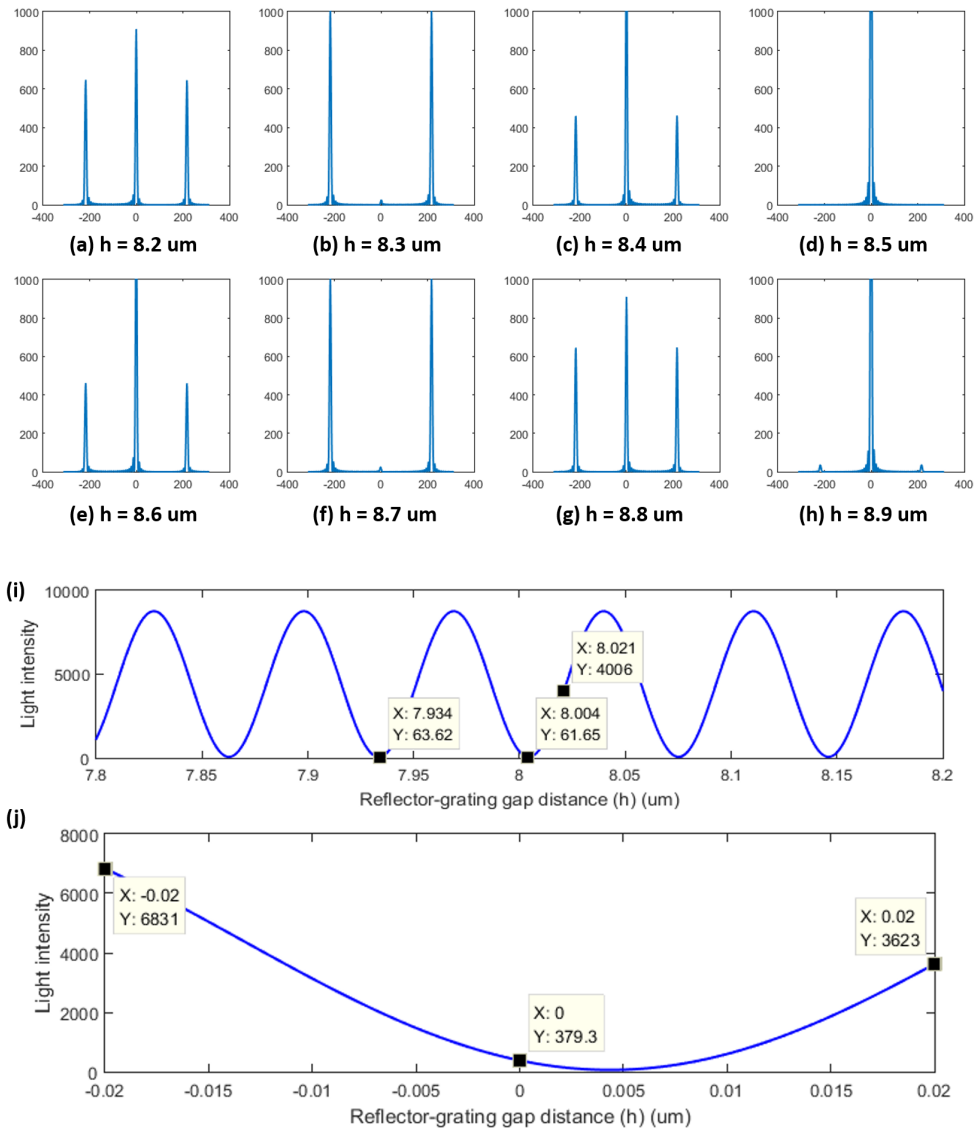
Figure 4.4: The reflector-grating gap distance increase from $8.2um$ to $8.9um$ (a to h). And the beam width is adjusted to $100um$. The tilt angle is 0, and other structural parameters are the same as in the Table 4.1. (i,j) The light intensity of the first diffracted order changes periodically with the vertical displacement.

can be reduced. Fortunately, for the Coriolis flow sensor involved in the project, the rotation angle of the reflection plane is on the scale of tens of milli-degrees. The size parameters set in this calculation example can meet the measurement requirements. For a certain tilt angle, the light intensity changes of the positive and negative first diffracted orders are opposite. When comparing the periodic changes of the optical signals of each group, a phase difference appears.

In addition, to facilitate the adjustment of parameters to obtain different diffraction results, a GUI is realized through Matlab programming, as shown in Figure 4.6. The partly key codes are introduced in the Appendix B.

4.3 FDTD method optical simulation

This section introduces the modeling and optical simulation through ANSYS Lumerical software, using the FDTD method. Firstly, the simulation results of double grating diffraction are compared with the numerical calculation results, which proves the correctness of the numerical calculation and the credibility of the simulation. Secondly, by modifying the geometric parameters and shapes of the grating, the appropriate size of each structure in the measurement system is summarized to provide a reference for the grating preparation and experiment.

4.3.1 Modeling and boundary condition setting

The optical simulation of the project uses the FDTD simulator in Lumerical software, which can accurately model and calculate for micro-nano optics. The structure of the simulation model is shown in the Figure 4.8. The detailed parameter settings for modeling and simulation are shown in Table 4.2.

In order to reduce the amount of calculation and improve the efficiency of simulation, the model was simplified reasonably. The incident light source is set as plane wave, with the same intensity and phase along the direction of grating fingers extension direction (y direction). Therefore, the diffraction effect corresponding to each diffraction angle is uniformly distributed in the y direction, except for the two ends. The purpose of this simulation example is to verify the distribution and variation of diffracted orders along the x-direction. So, the computational domain only intercepts a very thin slice, which greatly reduces the overall calculation amount. The materials of the grating and the reflecting mirror are both perfect electric conductor (PEC),
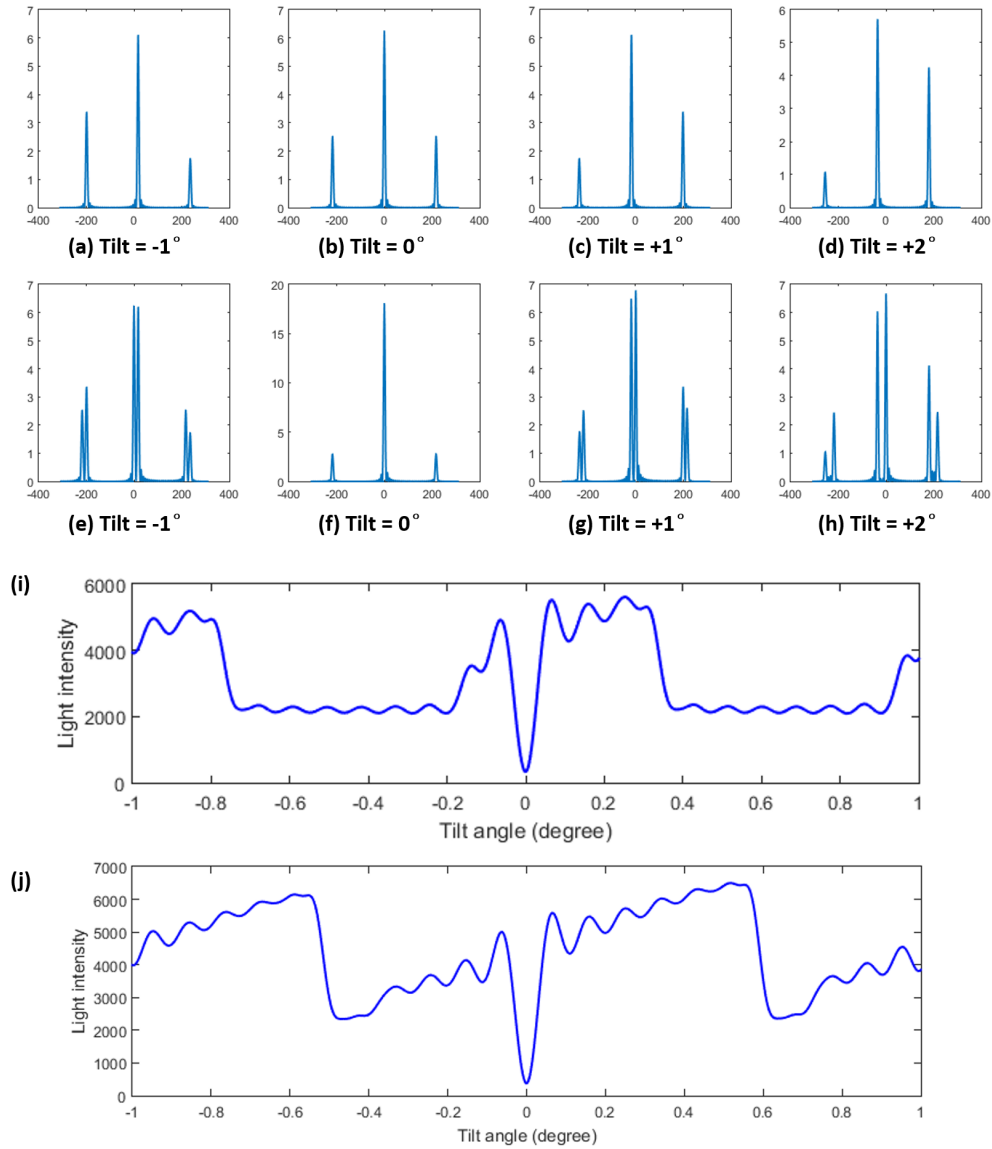
Figure 4.5: The tilt angle of reflector increases form -1 degree to $+2$ degree. Other structural parameters are the same as in the Table 4.1. (a-d) The light field of the transmission grating, with different tilt angles. (e-h) The light field of the double diffraction grating interference result. (i,j) According to the diffraction angle of the first diffracted order when the tilt angle is 0 degrees, working distance is $1000um$. Integral range of total light intensity is (i) from $+200um$ to $+250um$ and (j) from $+150um$ to $+300um$.
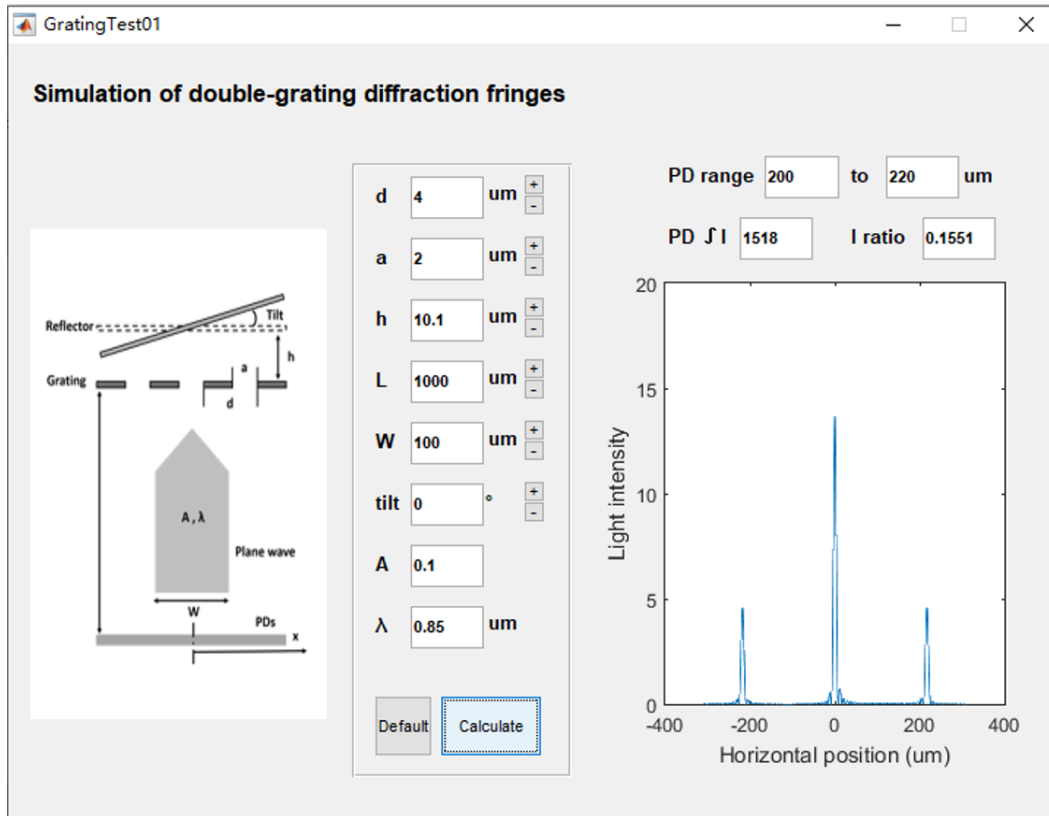
Figure 4.6: The Matalb GUI for diffraction numerical calculation.

Table 4.2: The parameters of the double grating structure model for optical simulation

Parameter	Value
Wavelength of light source (λ)	$850nm$
Grating period (d)	$4um$
Grating slit width (a)	$2um$
Grating slit length	$400um$
Distance from grating to reflector (h)	$0.5um$
Distance from grating to photodetector (L)	Far field projection
Light beam width (W)	$600um$
Light amplitude constant (A)	1
FDTD region (x,y,z)	$400 \times 0.5 \times 2um$
Background material refractive index	1(vacuum)
Far field material refractive index	1(vacuum)

which has complete reflection and zero absorption of the incident electric field.

The boundary condition of the FDTD calculation domain is set to a perfect metal layer (PML), which has complete absorption of the electric field and prevents reflection. Also, reasonable selection of the symmetry boundary conditions according to the polarization direction of the light source can reduce the calculation amount by half. When the overall structure and the polarization of the light source have the same symmetry, the electric and magnetic fields (EM fields) will obey certain symmetry rules with respect to reflections through the plane of symmetry. The reflection symmetry rules are shown in the Figure 4.7. When the polarization direction is parallel to the symmetry plane, select the symmetry boundary condition. When the polarization direction is perpendicular to the plane of symmetry, the anti-symmetric boundary condition is selected.
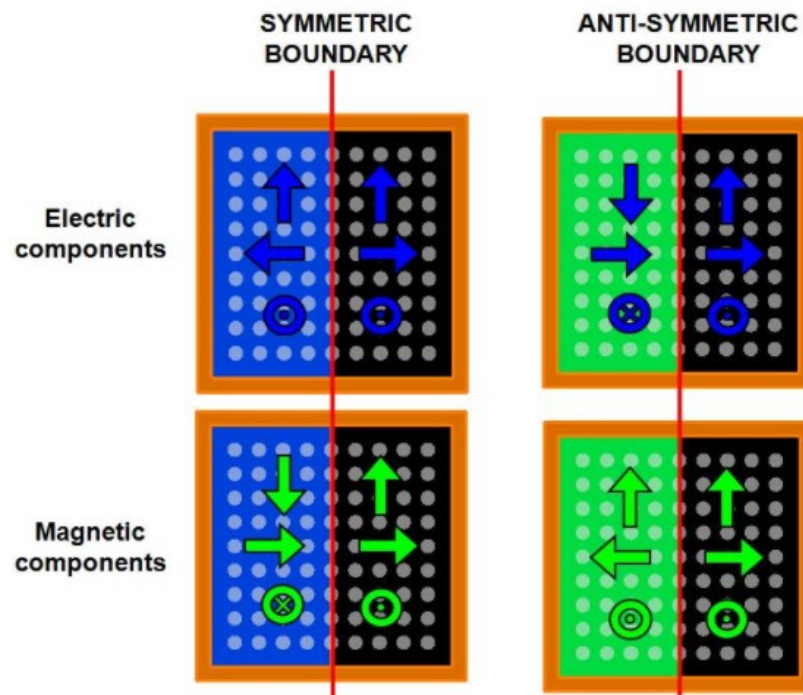
Figure 4.7: Comparison of the symmetry/anti-symmetry boundary conditions for the direction of the EM fields vector.

Since the polarization of the plane wave in our model is along the x-axis, the x-axis and y-axis are set with anti-symmetric boundary conditions and symmetric boundary conditions, respectively. The final simulation calculation amount and memory requirement are reduced to a quarter.
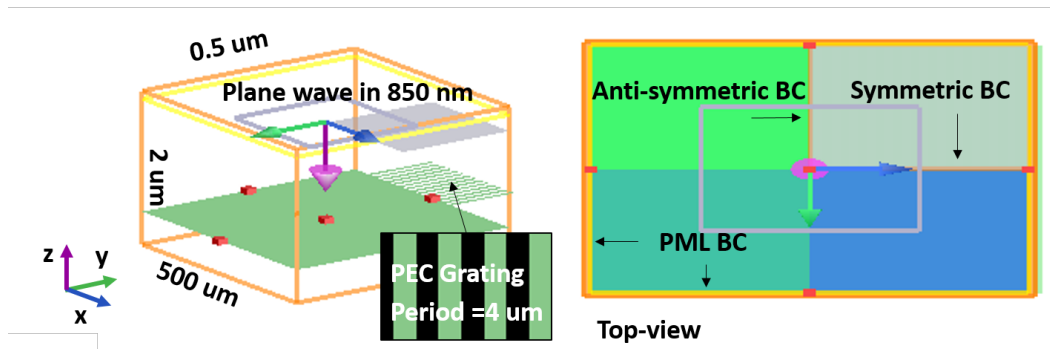
Figure 4.8: Modeling in FDTD optical simulation software, Ansys Lumerical.

## 4.3.2   Simulation result analysis

After setting the relevant parameters of the grating and light source, the result of double grating diffraction can be calculated. To reduce the amount of calculation, the FDTD calculation domain is only limited in the space where the grating and mirror are located.

In practical applications, the plane where the light source and light detection are located is far away from the grating. So the far-field projection function is used to process the simulation results. The far-field projection function can sample and decompose the near-field electromagnetic field data in the different angles. The end result is that the far field projections functions provide a straightforward, accurate, and numerically efficient method for calculating the electromagnetic fields anywhere in the intermediate and far field regions. For the diffraction model, a certain light propagation distance is required to separate the diffracted orders. As shown in the Figure 4.9, the light field in the near field is obviously concentrated at the grating stripes and slits. The two groups of diffracted fields have a certain phase difference. Although the superposition effect can be displayed, the obvious diffracted order cannot be distinguished. The corresponding far-field projection results show that the diffracted orders are clearly separated, and the corresponding positions and diffraction angles are equal to the theoretical calculations.

By adjusting the distance between the mirror and the grating, the diffraction effect changes as shown in the Figure 4.10. The intensity distribution and change trend of the first diffracted order have similarities with numerical calculations.

While the values of the zeroth order in the simulation are higher than these form calculation. The one possible reason for this difference is that the meshing of the two calculation modes is different. In the FDTD simulation, the calculation cells are set as mesh with certain length in x, y and z directions. In our calculation case, the mesh accuracy is set as $0.05um$. While in the mathematical calculation process, the
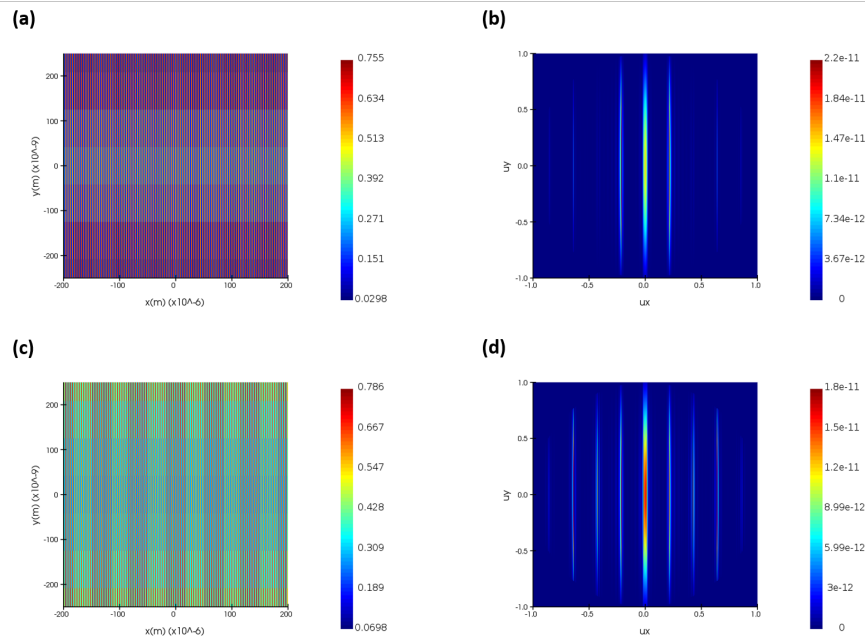
Figure 4.9: FDTD simulation results of the near-field and far-field projections of the diffraction effect of the reflective grating(a,b), and the double grating model(c,d).

overall light field is calculated by the differential diffraction angle. So there is no iterative calculation between calculation units in finite element simulation. Therefore, some possible accumulation of errors will cause deviations between simulation and calculation.

The other possible reason for difference between calculation and simulation is the start plane position of the diffracted field of the transmission grating. In the mathematical model of the double grating diffraction model, the starting plane of the diffraction grating and the transmission grating are the same, and the overall light intensities are equal (when the grating ratio is 0.5). But in the simulation model, which is closer to the real physical model, the plane wave beam passing through the front of the grating slit will also produce diffraction. These transmitted sub-beams will have a divergence angle, and cause the light beam reflected by the mirror to be partially blocked by the back of the grating. As a result, the total light intensity of the transmission grating diffracted field will be less than that of the reflective grating diffracted field.

For the design of the optical readout system using the double grating model, the zeroth diffracted order cannot be detected. So more important is the light intensity distribution and change law of the first diffracted order. For this, the results of optical simulation can be used to prove the feasibility and accuracy of the derived diffraction formula. Therefore, the subsequent structural design is based on the results of

numerical calculations.
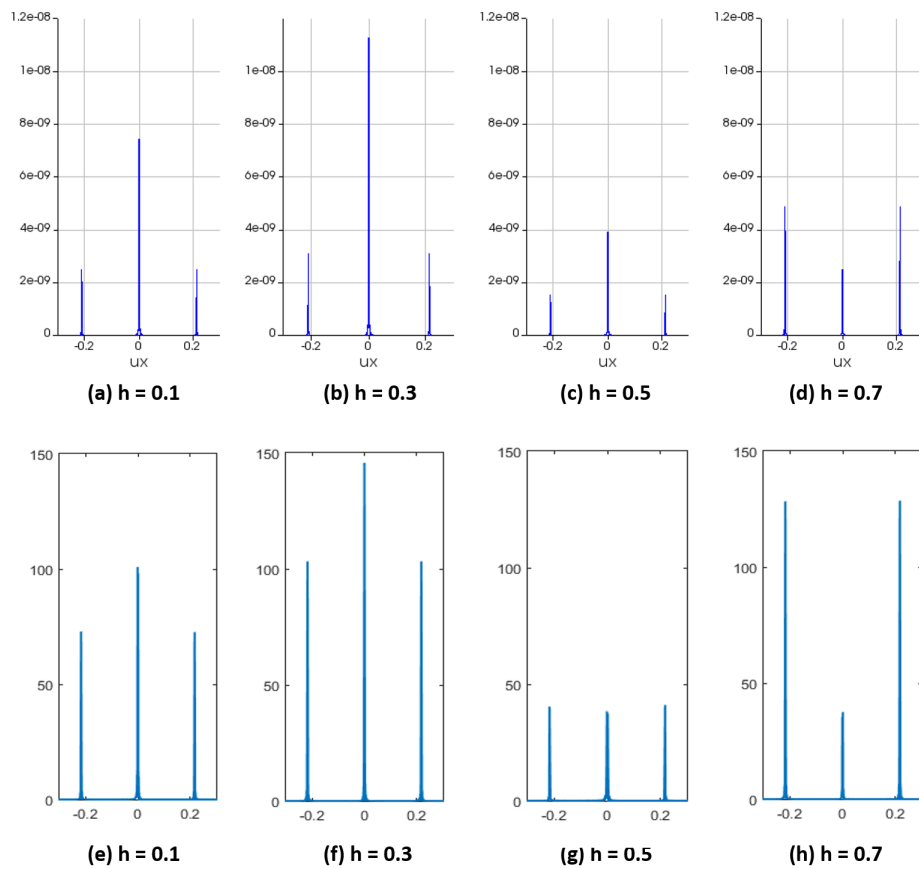
Figure 4.10: Optical simulation (a-d) and mathematical calculation (e-h) results of the double grating diffraction model, the mirror-grating interval is from 0.1 to $0.7um$.

4.4   Evaluation and feasibility analysis

Phase shift detection method is used to map the phase difference of the periodic optical signals of the two PDs to the amplitude of the Coriolis movement. In the numerical calculation, the light intensities corresponding to the positive and negative first diffracted orders are respectively integrated, displayed in the time domain as two optical signals, as shown in the Figure 4.11(a-d).

The phase difference corresponding to the two signals will shift with the change of the vertical motion amplitude. Based on the results shown in the Figure 4.11(e),
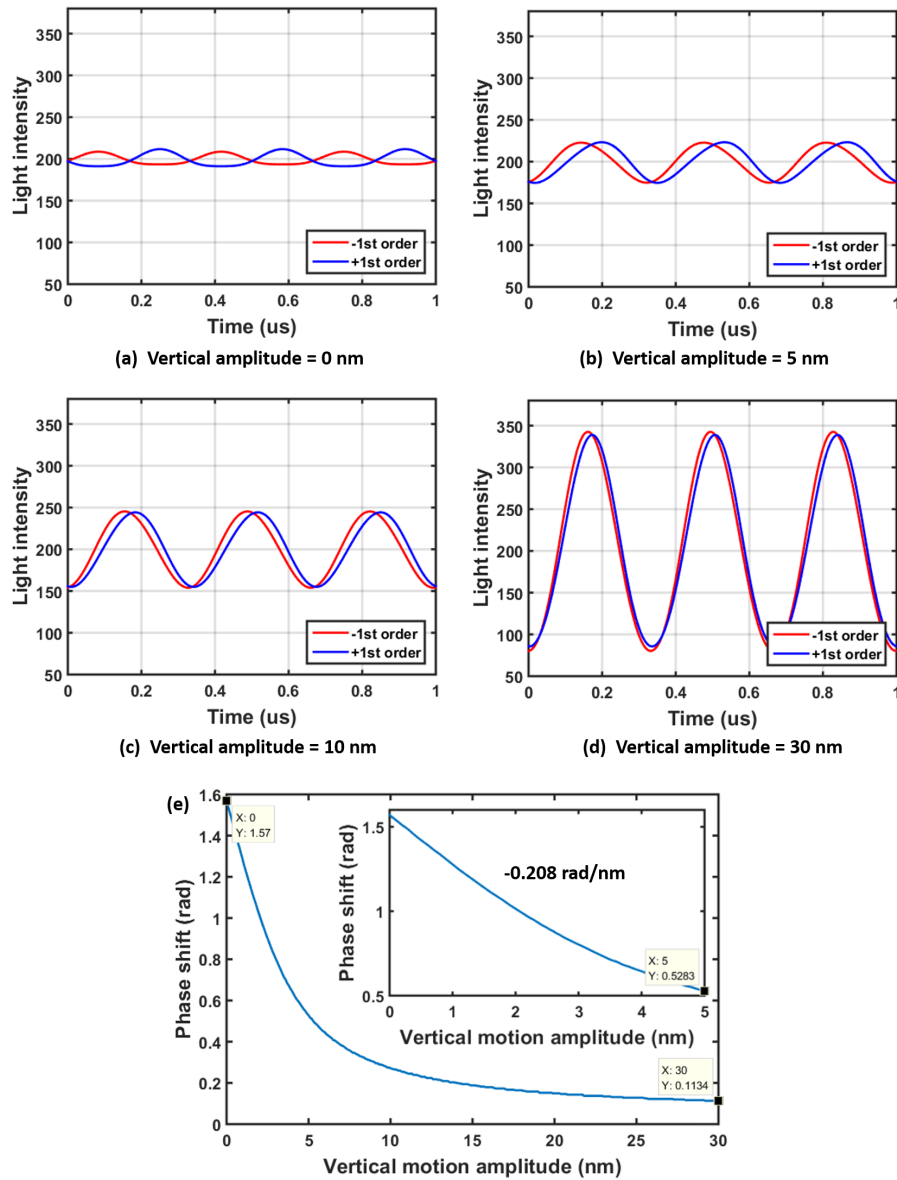
Figure 4.11: The phase shift calculation for double grating structure, when rotational amplitude is 0.034 degrees, same as the technical requirement in the Table 1.1, and the vertical amplitude is form 0 to $50nm$.

the sensitivity and test range of this system can be evaluated. In the vertical amplitude range of 0 to $5nm$, the detection can maintain linearity with a sensitivity of $-0.2083rad/nm$. When the vertical amplitude continues to increase, the response curve shows non-linear, and the final phase difference tends to a stable value of $0.1134rad$. Refer to the graph of the response of light intensity in the Figure 4.4 and the Figure 4.5, the reason for the non-linearity is the mismatch of the influence of the two motion amplitudes. Specifically, the change rate of light intensity corresponding to a 0.034 degrees rotating motion is about one-fourth that of a $30nm$ vertical motion. This results in that when the vertical movement amplitude is large (over $10nm$ in this case), it will become the main determinant of light intensity. Since the vertical motion synchronously effect the positive and negative first diffracted orders, the phase shift eventually tends to a constant value. This tiny inherent phase difference comes from the geometric asymmetry of the grating in the mathematical model.

Therefore, by increasing the driving power and reasonably increasing the amplitude of the initial rotary motion, the linear response range can be expanded. According to the range of the "blind zone" in the Figure 4.5, the maximum rotation detection range is 0.4 degrees, corresponding to the $17.45um$ displacement at the corner of the micro-tube loop. The obtained linear region of phase shift is significantly enlarged to $12nm$, as shown in the Figure 4.12. The step-shaped turning point deviating from the fitted phase shift curve corresponds to the small fluctuations in the rising curve of $-0.4 - 0$ and $0 - 0.4$ degrees in the Figure 4.5(j).

However, when the linear range is increased by increasing the amplitude of the rotational movement ($0.05 - 0.4$ degrees), the sensitivity will decrease. When the amplitude is 0.4 degrees, the sensitivity is $0.008rad/nm$. When the amplitude is 0.3 degrees, the sensitivity is $0.014rad/nm$, with a linear range of $7.6nm$. Therefore, in the subsequent design of this readout system, the initial drive power should be adjusted according to the range to be detected and the sensitivity of the signal-processing circuit.

Overall, the feasibility of the optical readout system based on the double grating structure has been verified by numerical calculations and optical simulations. However, there are still three issues that affect the detection range and accuracy of the system.

- First, when the reflector rotates, the light intensity change of the first diffracted order corresponding to the rotation angle, which is nonlinear. It poses a challenge to the phase calibration.
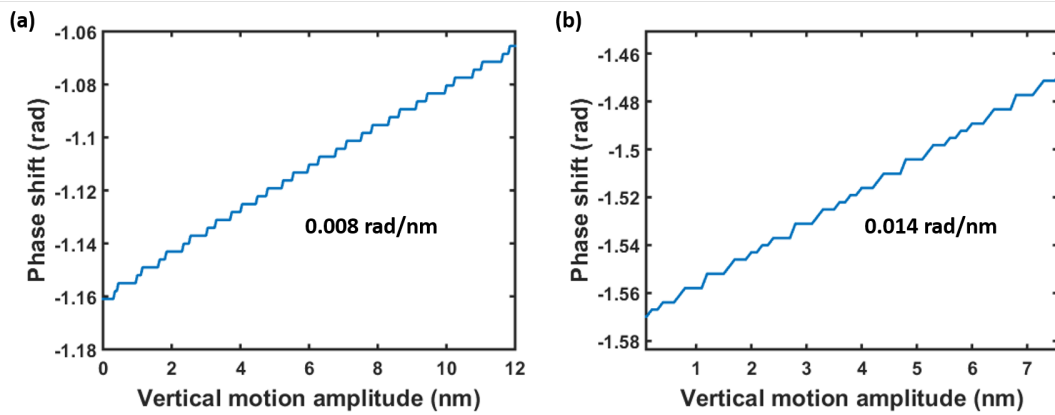
Figure 4.12: The phase shift calculation when rotational amplitude is (a) 0.4 and (b) 0.3 degrees.

- Second, the structural parameters have a greater impact on the results. For example, the grating-mirror spacing, the grating ratio, etc. Due to optical diffraction and interference occur on the sub-micron scale, the micron-level structural errors will have impact on the final light field distribution. These structural error will come from the alignment of source and detector to the reflecting structure or fabrication process. For the phase shift measurement method used, the error of the tilt angle mainly affects the contour of the baseline. So the calibration of the signal peak value needs to be adjusted accordingly. For the error of the grating-mirror spacing, it will affect the deviation of the initial phase, which is an inherent error of the system. This error can be eliminated in the phase difference calculation process.

- Third, in order to ensure that the baseline of the initial rotational motion has an easily distinguishable and statistical profile, it is necessary to make the rotation angle at the millidegree level, refer the Figure 4.5. As described above, this will eventually weaken the vertical displacement (for the same mass flow). So the overall measurement sensitivity will be weakened. In this regard, the angular velocity and Coriolis force can be increased by increasing the driving frequency. Because the driving frequency must match the intrinsic frequency of the structure, the device structure needs to be fine-tuned. However, the existing capacitors can be used as a force control system. By providing a certain voltage to the capacitor, the comb-shaped electrode-plates will provide a viscous force to the movement of the device under the action of electrostatic force, thereby changing the intrinsic frequency appositive and negative first-order and damping coefficient of the structure. More in-depth details are not included in this thesis.

Experimental testing

This chapter briefly introduces the experimental testing platform, including devices selection and related processes of grating preparation. The test mainly focuses on the influence of small displacement on the diffraction effect, and verifies the feasibility of optical readout method.

5.1 Devices of test platform

5.1.1 Grating and reflector

The project first adopted a photolithography mask as the carrier of the grating. Patterned chromium layer on a $2mm$ glass substrate. As shown in the Figure 5.1, grating cells with different directions, and different grating periods are set on a $5 - inch$ photomask.
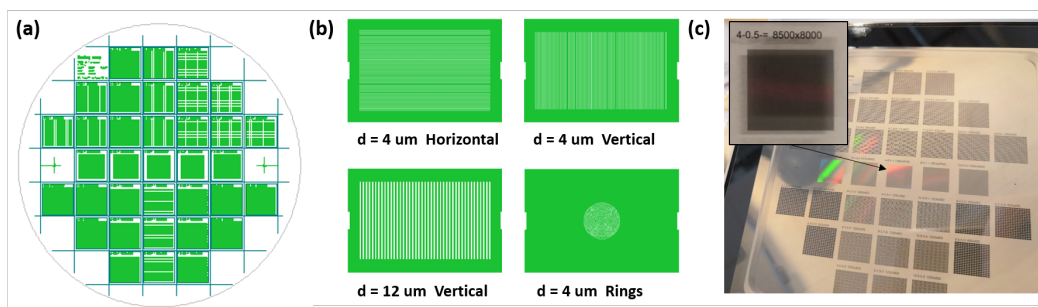
Figure 5.1: The layout of photomask with different kinds of grating.

According to the diffraction formula, different grating periods can adjust the spacing of the diffracted orders to match the size and layout requirements of the experimental device. The ring-shaped grating will form concentrically distributed diffracted

orders [45], which can improve the error tolerance of the position accuracy of the PDs, as shown in the Figure 5.2.
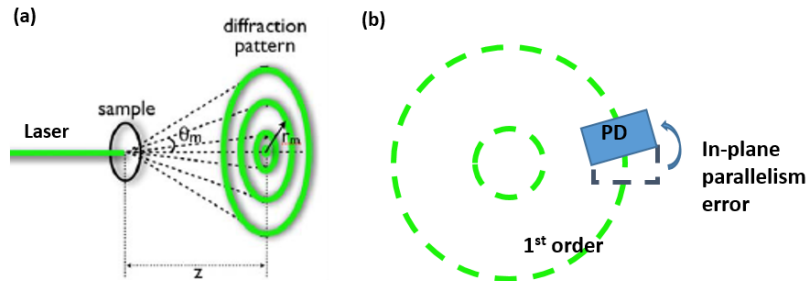
Figure 5.2: (a) Sketch of the diffraction pattern produced by a circular diffraction grating when illuminated with coherent light and (b) light sensor position error tolerance.

The reflector is made of gold-deposited silicon chips and driven by the bonded piezoelectric ceramic chips to generate periodic vibrations in certain frequencies. Through the vibration meter to detect the displacement of the mirror under different driving frequencies, it can be known that the resonance frequency is about $2kHz$, which reaches the maximum amplitude.

5.1.2 Light source and PDs

Two different light sources are used in the experiment of the thesis, a laser diode with a wavelength of $850nm$ and a VCSEL diode with a wavelength of $850nm$. The smaller device size can facilitate the building of the experimental platform. The laser generator can provide a laser beam with a higher power $(>10mW)$ to meet the light intensity attenuation for the long light path. However, the beam has a large divergence angle. So a lens needs to be introduced to focus the beam in subsequent experiments.

The photodetector element is a photosensitive diode. It can be fixed by 3D printed structural parts and keep a certain distance from the central light source $(6mm)$, as shown in the Figure 5.3. Therefore, by changing the working distance, the photodetector can be located at the position of the first diffracted order spot, and the light intensity signal can be obtained.
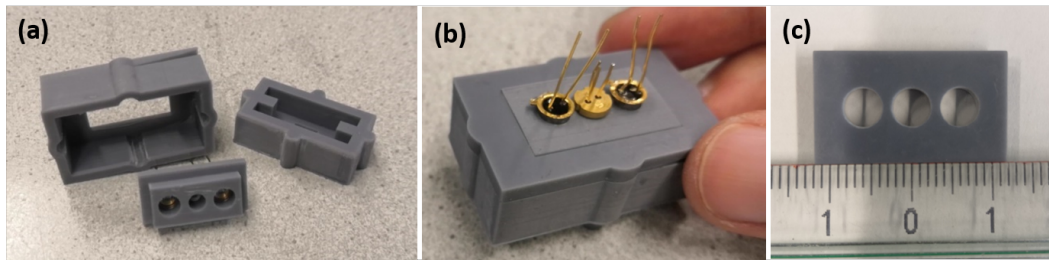
Figure 5.3: 3D printed parts, as a frame for fixing the device and shielding from external light interference.

5.2 Measurement

The signal readout process of the overall optical system is shown in the Figure 5.4. The transresistance amplifier is used to gain the overall optical signal, which is conducive to the measurement of signal changes. The low-pass filter can suppress high-frequency noise and can be achieved by software, like LabVIEW. Finally, through data acquisition, the periodic change and phase shift of the optical signal are measured.

Based on this, different detection experiments were carried out to verify whether the influence of the two motions in the double grating structure on the optical signal can be sensitively detected.
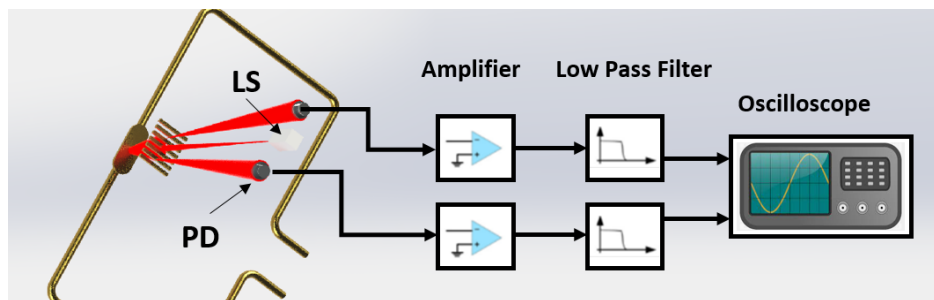
Figure 5.4: Schematic diagram of the optical signal readout system. In the preliminary experiment setup, the flow sensor part is also replaced with a gold-deposited reflector, driven by a piezoelectric device.

5.2.1 Testing platform I

The layout of the testing platform is shown in the Figure 5.5. The light source selects a laser diode with a wavelength of $850nm$, and keeps a distance of $6mm$ from the

photodetector. The selected grating period is $4um$. Estimated by the grating formula, Equation(4.1), when the working distance is $28.24mm$, the first diffracted order will be located at the position of the photodetector.

Figure 5.5: Optical testing platform with the 850 nm wavelength laser diode.

Remove the mirror and only detect the diffraction effect of the reflection grating. By adjusting the distance between the light source plane and the grating plane from $23.5mm$ to $33mm$, the optical signal has a peak value when the working distance is around $26mm$. The deviation between the measured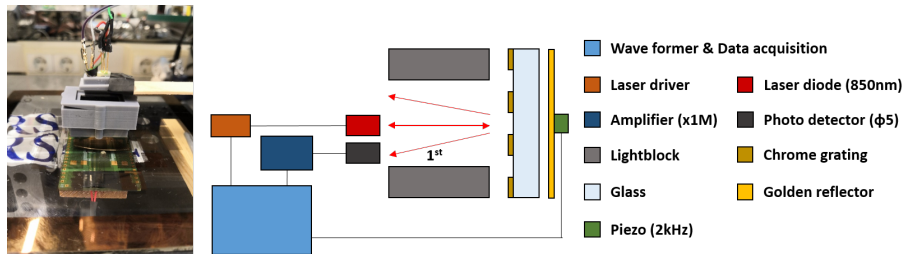 working distance and the theoretical value ($28.24mm$) may come from the angle between the grating and the detection plane.

Fixing the position of the light source and the grating, and set a reflector on the back of the photomask. The reflector and the glass substrate are separated by about $1mm$ and kept parallel. Use $5V$, $2kHz$ and sinusoidal signals to drive the piezoelectric film and drive the reflector to vibrate. The detected light intensity signal has not changed, as shown in the Figure 5.6.

Figure 5.6: Optical testing result with the $850nm$ wavelength laser diode and vibrated reflector.

There are two possible reasons for the failure of this experiment:

- First, the power of the laser diode is limited, which causes serious energy attenuation in the process of transmitting the glass substrate, and the light intensity of the transmission grating is too weak.

- Secondly, the piezoelectric driven reflector is tested by using a vibrometer. In the driving mode of $5V$, $2kHz$, the maximum vertical displacement is about tens of nanometers. Therefore, the light intensity change caused too small to be measured by the selected detection instrument, or be covered by noise.

Based on these analyses, the test platform was adjusted by shortening the distance between the light source and the light detector and adding the amplifier.

5.2.2 Testing platform II

Commercial VCSEL laser diode devices usually adopt a three-pin package and integrate PDs, which feed-back the light intensity signal irradiated by the laser diode to the peripheral drive circuit to monitor and regulate the drive power. This experimental platform uses a commercial VCSEL laser diode as a light source, and uses its integrated PDs as the sensitive element. The overall test platform layout is shown in the Figure 5.7.
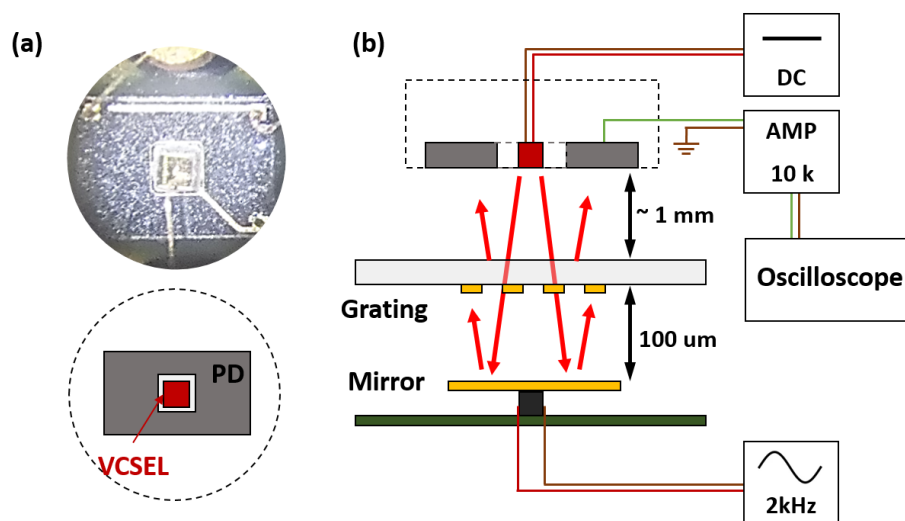
Figure 5.7: (a) The layout of the VCSEL laser diode. (b) Optical testing platform with the $850nm$ VCSEL laser diode and the grating (grating period is $4um$).

Through the Fast Fourier Transform (FFT) analysis of the raw detected signal, the complex signals can be decomposed into sinusoidal signals of different frequencies that are superimposed on each other. As shown in the Figure 5.8, the signals around $100Hz$ correspond to low-frequency noise, which occurs from the driving circuit of

the laser source or the environmental vibration of the test bench. The signals consistent with the driving frequency of the reflector are also showing obviously peaks responding to the impact of reflector's vertical displacement. And the peaks' value map the displacement amplitude (adjusted by driving voltage). Measured by the vibrometer, the amplitude of the reflector is 14.75, 35.63 and $50.37nm$, corresponding to the driving voltage of 3, 6 and $9V$. As the light source approaches the grating or the driving voltage is increased, the optical signal increases.

In this set of experimental results, the light intensity is related to the length of the transmission path, which is hard to prove the interference effect of the expected diffracted light field. But it can reflect the optical readout system's ability to detect changes in the optical signal generated by the high-frequency displacement, to provide guidance for subsequent experimental measurements.

5.3 Results analysis

Preliminary experiments have proved that the diffracted order position accords with the theoretical calculation result. It is worth noting that the refraction at the interface of the optical medium will cause positional errors. However, in the device structure design introduced in the previous chapter, the light source exit plane and the sensitive surface of the PDs array are both attached to the glass substrate. This results in two sets of diffracted light fields propagating in a single medium.

In addition, the experiment also proved that the change of the optical field distribution caused by the high-frequency periodic displacement of the reflector can be detected and measured by the PDs and signal processing circuits. This provides a reference for the actual measurement of the fabricated device.

However, there is no convincing evidence in the experiment to show whether the two sets of diffraction gratings interfere with each other as expected. Subsequent experiments need to solve two problems to improve the stability and reliability of the test platform.

First, as introduced in the previous chapter, the diffracted light field of the transmission grating is very sensitive to the tilt angle of the mirror. Even with a small initial angle error, manually controlling the position and angle of each component will cause the diffracted orders of the two sets of diffracted light fields to no longer overlap, thereby affecting the interference effect, as shown in Figure 4.5(a-h). If the interference effect of the two sets of diffraction fields is weakened or even does not occur, the vertical displacement driven by the piezoelectric ceramics will hardly change the light intensity of the diffracted orders. Therefore, it is necessary to accurately control
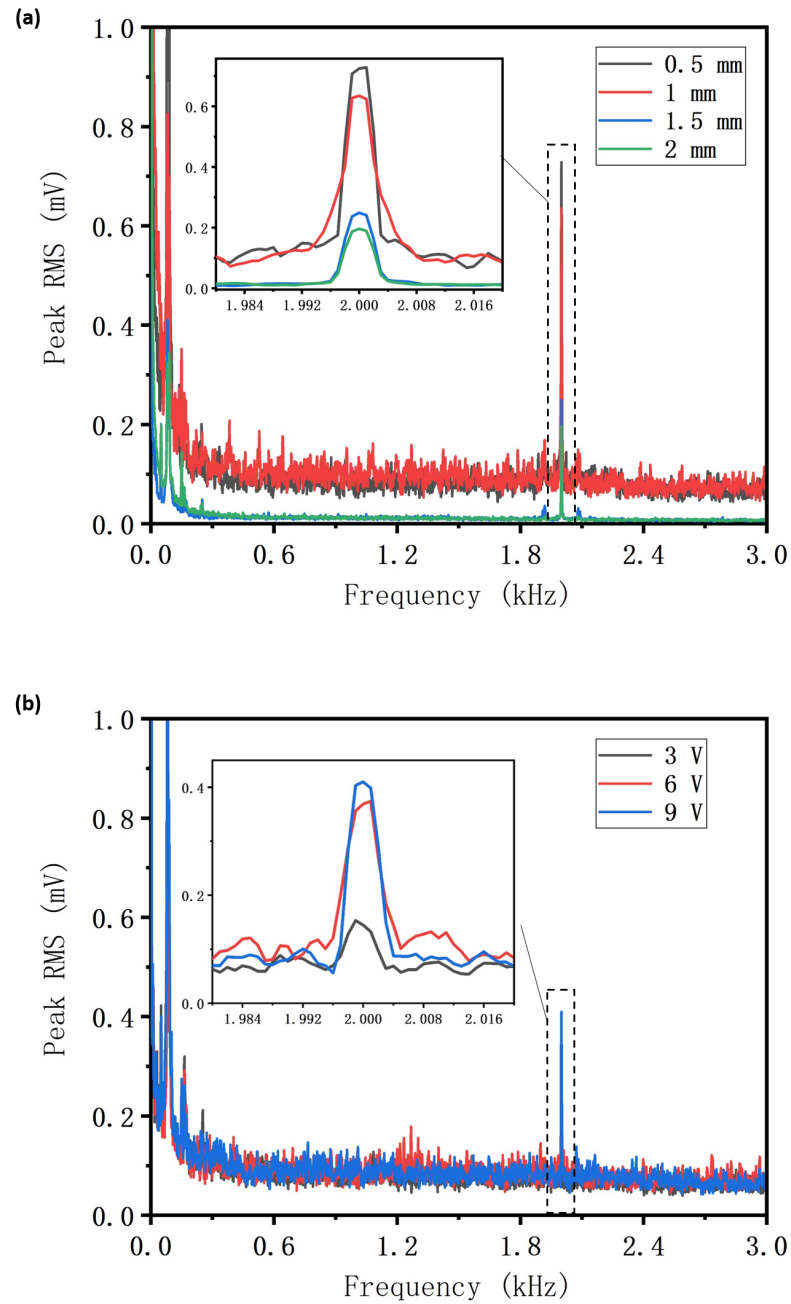
Figure 5.8: FFT analysis result. The reflector is driven by the piezo with a $2kHz$ sin-wave power supply. (a) The distance form the laser diode to the top-surface of the mask is form 0 to $1.5mm$ (piezo driven voltage is $6V$). (b) The piezo driven voltage is form 3 to $9V$ (distance form the laser diode to the top-surface of the mask is $0.5mm$).

the parallelism of the initial layout of each device layer. For the assembly of separate parts, CCD or macro camera can be used to check the diffraction pattern in real time, which can be used as a reference for manual adjustment. For the on-chip integrated processing structure, the parallelism is mainly controlled by the process, and usually can have a sufficiently high precision.

Second, shorten the optical transmission path to reduce transmission loss and environmental noise. This requires the integration of smaller laser diodes and PDs dies to maintain micron-level spacing.

Chapter 6

Conclusions And Recommendations

6.1 Conclusions

The thesis designs an optical micro-displacement readout method for a Coriolis mass flow sensor. The measurement system uses the surface of the suspended movable micro-tube as a reflector, and a fixed grating is set above it. When the incident laser beam is reflected by the metal grating surface and transmitted again after being reflected by the reflector, two sets of diffracted light fields are generated, which also interfere with each other. The phase difference between the two sets of diffracted light fields is determined by the light path difference, corresponding to the initial distance of the grating-reflector gap and the vertical/rotational displacement of the reflector. Therefore, the slight displacement of the reflector will determine the light intensity of the diffracted order of the compound diffraction field, which can be measured by the photodetectos to derive the displacement.

We have verified the theoretical feasibility of this optical readout system through the mathematical derivation and optical simulation of the double grating diffracted light field expression. Combined with the working principle of the flow sensor, when the reflector maintains a periodic rotation of 2 millidegrees, it has high sensitivity to composite vertical displacement. Through the phase-shifting analysis of the periodic optical signal, the system has linearity and a sensitivity of $-0.208 rad/nm$ within a vertical movement range of $5nm$. Also, this response characteristics can be adjusted by increasing the initial rotation amplitude in the rang form 2.18 to $17.45um$. In the Appendix C, through the vibrometer test, the initial amplitude of the flow sensor device meets the requirement.

Preliminary experimental attempts have verified that the light field changes caused by periodic nano-scale displacements with high frequency can be recorded and measured by the photodetector. Also, based on the research results, the devices' parameter selection and overall layout of the optical readout system, including the photomask, were designed. However, due to the high requirements for the position

accuracy of the overall structure of the device, the preparation and actual test of the device integrating the various components are still necessary to strictly verify the feasibility.

This optical readout method based on double grating diffraction has a simple structure and a high degree of integration, and is easily combined with the original structure of the flow sensor involved. Theoretical research and published actual measurement conclusions of similar structures have proved its potential worthy of follow-up in-depth research and testing.

6.2   Recommendations

Combined with the above conclusions, there are two main aspects that currently need to be optimized for confirmatory experiments.

1. Experiments based on driven mirrors need to design more suitable driving methods or more stable posture adjustment fixtures. The current piezoelectric drive method cannot achieve precise control of micron-level displacement or rotation. Moreover, the parallelism of the device is hardly accurately controlled, which has a decisive influence on the position of the diffracted order and whether interference occurs. Therefore, more precise fixtures or experimental platforms are needed.

2. Adjust the structural parameters in the theoretical model and summarize the tolerance of the inspection system characteristics to the tolerances of the machining process. For the structural layout designed in Chapter 3, the potential processing error exists in the parallelism and spacing between the sensor device layer and the glass substrate, which will cause the initial optical path difference of the two sets of diffracted light fields to change. Therefore, it is necessary to add more theoretical calculations to analyze the influence of tolerances or propose methods to compensate for the errors.

In addition, there are still points worthy of further research and discussion on the structural design.

1. Adjust the light field by changing the grating layout. The designed grating structure can be realized by patterning the metal layer deposited on the substrate, which provides a high feasibility to design more complex grating structures, resulting in more complex diffraction patterns. For example, a matrix grating will obtain an array of diffracted orders distributed in two vertical directions on the plane. Therefore, the tilting movement of the reflector can be measured in

two dimensions. Through reasonable comparison and calculation, it has great potential to improve sensitivity.

2. Introduce a reference light detector. Since the pattern corresponding to the designed grating is stripe-shaped, a light sensor can be also set in the PD3 position, as shown in the photomask design Figure 4.2,to measure the zeroth diffracted order light intensity signal. This signal has the potential to be used as a reference signal to analyze changes in the overall light field intensity. And then as a feedback signal to adjust the drive-power of the light source to make the light stable.

3. Reference literature review, optimize the detection characteristics of the optical system by methods introduced in Chapter 2, such as multi-wavelength light sources.

Bibliography

[1] J. Haneveld, T. S. Lammerink, M. J. de Boer, R. G. Sanders, A. Mehendale, J. C. Lötters, M. Dijkstra, and R. Wiegerink, "Modeling, design, fabrication and characterization of a micro coriolis mass flow sensor," *Journal of micromechanics and microengineering*, vol. 20, no. 12, p. 125001, 2010.

[2] T. V. Schut, R. J. Wiegerink, and J. C. Lötters, "μ-coriolis mass flow sensor with differential capacitive readout," *IEEE Sensors Journal*, vol. 21, no. 5, pp. 5886–5894, 2020.

[3] T. Schut, R. Wiegerink, and J. Lötters, "μ-coriolis mass flow sensor with resistive readout," *Micromachines*, vol. 11, no. 2, p. 184, 2020.

[4] "-coriolis mass flow sensor with improved flow sensitivity through modelling of the sensor," *Microelectronic Engineering*, vol. 226, p. 111289, 2020.

[5] L. Kristiansen, A. Mehendale, D. M. Brouwer, J. Zwikker, and M. Klein, "Optical measurement of a micro coriolis mass flow sensor," in *9th EUSPEN International Conference 2009*, 2009, pp. 328–332.

[6] D. J. Bell, T. Lu, N. A. Fleck, and S. M. Spearing, "Mems actuators and sensors: observations on their performance and selection for purpose," *Journal of Micromechanics and Microengineering*, vol. 15, no. 7, p. S153, 2005.

[7] D. K. Shaeffer, "Mems inertial sensors: A tutorial overview," *IEEE Communications Magazine*, vol. 51, no. 4, pp. 100–109, 2013.

[8] H. Xie and G. K. Fedder, "Vertical comb-finger capacitive actuation and sensing for cmos-mems," *Sensors and Actuators A: Physical*, vol. 95, no. 2-3, pp. 212–221, 2002.

[9] M. A. Haque and M. Saif, "A review of mems-based microscale and nanoscale tensile and bending testing," *Experimental mechanics*, vol. 43, no. 3, pp. 248–255, 2003.

[10] R. G. Dorsch, G. Häusler, and J. M. Herrmann, "Laser triangulation: funda-
     mental uncertainty in distance measurement," *Applied optics*, vol. 33, no. 7, pp.
     1306–1314, 1994.

[11] M. Flood, "Laser altimetry: From science to commerical lidar mapping," *Pho-
     togrammetric engineering and remote sensing*, vol. 67, no. 11, 2001.

[12] Y. Shao, D. L. Dickensheets, and P. Himmer, "3-d moems mirror for laser beam
     pointing and focus control," *IEEE Journal of Selected Topics in Quantum Elec-
     tronics*, vol. 10, no. 3, pp. 528–535, 2004.

[13] H. Sagberg, A. Sudbo, O. Solgaard, K. Bakke, and I. Johansen, "Optical mi-
     crophone based on a modulated diffractive lens," *IEEE Photonics Technology
     Letters*, vol. 15, no. 10, pp. 1431–1433, 2003.

[14] I. Ishikawa, R. Sawada, E. Higurashi, S. Sanada, and D. Chino, "Integrated
     micro-displacement sensor that measures tilting angle and linear movement
     of an external mirror," *Sensors and Actuators A: Physical*, vol. 138, no. 2, pp.
     269–275, 2007.

[15] J.-A. Kim, K.-C. Kim, E. W. Bae, S. Kim, and Y. K. Kwak, "Six-degree-of-
     freedom displacement measurement system using a diffraction grating," *Re-
     view of Scientific Instruments*, vol. 71, no. 8, pp. 3214–3219, 2000.

[16] A. Smith and C. Hause, "Fraunhofer multiple slit diffraction patterns with finite
     sources," *JOSA*, vol. 42, no. 6, pp. 426–430, 1952.

[17] P. Munshi, A. Ø. Madsen, M. A. Spackman, S. Larsen, and R. Destro, "Es-
     timated h-atom anisotropic displacement parameters: a comparison between
     different methods and with neutron diffraction results," *Acta Crystallographica
     Section A: Foundations of Crystallography*, vol. 64, no. 4, pp. 465–475, 2008.

[18] D. Guo, L. Shi, Y. Yu, W. Xia, and M. Wang, "Micro-displacement reconstruction
     using a laser self-mixing grating interferometer with multiple-diffraction," *Optics
     express*, vol. 25, no. 25, pp. 31 394–31 406, 2017.

[19] S. Tang, Z. Wang, J. Gao, and J. Guo, "Measurement method for roll angular
     displacement with a high resolution by using diffraction gratings and a hetero-
     dyne interferometer," *Review of Scientific Instruments*, vol. 85, no. 4, p. 045110,
     2014.

[20] Q. Lu, J. Bai, K. Wang, P. Chen, W. Fang, and C. Wang, "Single chip-based
     nano-optomechanical accelerometer based on subwavelength grating pair and
     rotated serpentine springs," *Sensors*, vol. 18, no. 7, p. 2036, 2018.

[21] O. Bochobza-Degani, R. Yechieli, S. Bar-Lev, U. B. Yehuda, and Y. Nemirovsky, "Characterization of a novel micromachined accelerometer with enhanced-midos," in *TRANSDUCERS'03. 12th International Conference on Solid-State Sensors, Actuators and Microsystems. Digest of Technical Papers (Cat. No. 03TH8664)*, vol. 2.   IEEE, 2003, pp. 1395–1398.

[22] B. Bicen, S. Jolly, K. Jeelani, C. T. Garcia, N. A. Hall, F. L. Degertekin, Q. Su, W. Cui, and R. N. Miles, "Integrated optical displacement detection and electrostatic actuation for directional optical microphones with micromachined biomimetic diaphragms," *IEEE Sensors Journal*, vol. 9, no. 12, pp. 1933–1941, 2009.

[23] J. D. Hamilton, T. Buma, M. Spisar, and M. O'Donnell, "High frequency optoacoustic arrays using etalon detection," *IEEE transactions on ultrasonics, ferroelectrics, and frequency control*, vol. 47, no. 1, pp. 160–169, 2000.

[24] N. Hall and F. L. Degertekin, "An integrated optical detection method for capacitive micromachined ultrasonic transducers," in *2000 IEEE Ultrasonics Symposium. Proceedings. An International Symposium (Cat. No. 00CH37121)*, vol. 1. IEEE, 2000, pp. 951–954.

[25] N. A. Hall and F. L. Degertekin, "Self-calibrating micromachined microphones with integrated optical displacement detection," in *Transducers' 01 Eurosensors XV*.   Springer, 2001, pp. 118–121.

[26] ——, "Integrated optical interferometric detection method for micromachined capacitive acoustic transducers," *Applied Physics Letters*, vol. 80, no. 20, pp. 3859–3861, 2002.

[27] N. A. Hall, M. Okandan, and F. L. Degertekin, "Surface and bulk-silicon-micromachined optical displacement sensor fabricated with the swift-lite™ process," *Journal of microelectromechanical systems*, vol. 15, no. 4, pp. 770–776, 2006.

[28] B. Kim, M. C. Schmittdiel, F. L. Degertekin, and T. R. Kurfess, "Scanning grating microinterferometer for mems metrology," *J. Manuf. Sci. Eng.*, vol. 126, no. 4, pp. 807–812, 2004.

[29] B. Kim, F. Degertekin, and T. Kurfess, "A micromachined scanning grating interferometer for the out-of-plane vibration measurement of mems," *Journal of Micromechanics and Microengineering*, vol. 17, no. 9, p. 1888, 2007.

[30] O. Karhade, F. Degertekin, and T. Kurfess, "Soi-based micro scanning grating interferometers: device characterization, control and demonstration of parallel operation," *Journal of Micromechanics and Microengineering*, vol. 18, no. 4, p. 045007, 2008.

[31] O. Ferhanoglu, M. F. Toy, and H. Urey, "Two-wavelength grating interferometry for mems sensors," *IEEE Photonics Technology Letters*, vol. 19, no. 23, pp. 1895–1897, 2007.

[32] B. Van Gorp, A. Onaran, and F. Degertekin, "Integrated dual grating method for extended range interferometric displacement detection in probe microscopy," *Applied Physics Letters*, vol. 91, no. 8, p. 083101, 2007.

[33] O. Karhade, L. Degertekin, and T. Kurfess, "Active control of grating interferometers for extended-range low-noise operation," *Optics letters*, vol. 34, no. 19, pp. 3044–3046, 2009.

[34] J.-y. Feng, X.-y. Ye, Y.-f. Shang, K. Wu, and F. Chen, "Integrated dual grating polymer microbeams for bio-chemical sensing in liquid environment," in *The 8th Annual IEEE International Conference on Nano/Micro Engineered and Molecular Systems*. IEEE, 2013, pp. 1204–1207.

[35] O. Ferhanoĝlu and H. Urey, "Sensitivity enhancement of bimaterial moems thermal imaging sensor array using 2-λ wavelength readout," in *Optical Micro-and Nanometrology III*, vol. 7718. International Society for Optics and Photonics, 2010, p. 77180O.

[36] O. Ferhanoglu and H. Urey, "Sensitivity enhancement of grating interferometer based two-dimensional sensor arrays using two-wavelength readout," *Applied optics*, vol. 50, no. 19, pp. 3289–3295, 2011.

[37] K. Wu, X. Ye, F. Chen, L. Liu, L. Guo, and Z. Zhou, "Micromachined interferometric accelerometer fabricated using sgader process," in *2009 4th IEEE International Conference on Nano/Micro Engineered and Molecular Systems*. IEEE, 2009, pp. 1058–1061.

[38] Z. Q. Z. Z. F. Lishuang and Y. Baoyin, "Research on optical structure of the novel micron-grating accelerometer," *Acta Optica Sinica*, p. 06, 2010.

[39] Y. Zhang, S. Gao, H. Xiong, and L. Feng, "Optical sensitivity enhancement in grating based micromechanical accelerometer by reducing non-parallelism error," *Optics express*, vol. 27, no. 5, pp. 6565–6579, 2019.

[40] S. Gao, Z. Zhou, Y. Zhang, K. Deng, and L. Feng, "High-resolution micro-grating accelerometer based on a gram-scale proof mass," *Optics express*, vol. 27, no. 23, pp. 34 298–34 311, 2019.

[41] S. Zhao, J. Zhang, C. Hou, J. Bai, and G. Yang, "Optical tilt sensor with direct intensity-modulated scheme," *Optical Engineering*, vol. 50, no. 11, p. 114405, 2011.

[42] Q. Lu, C. Wang, J. Bai, K. Wang, W. Lian, S. Lou, X. Jiao, and G. Yang, "Sub-nanometer resolution displacement sensor based on a grating interferometric cavity with intensity compensation and phase modulation," *Applied Optics*, vol. 54, no. 13, pp. 4188–4196, 2015.

[43] S. Odinokov, M. Shishova, A. Y. Zherdev, M. Kovalev, M. Galkin, and V. Y. Venediktov, "Modeling of phase shifts of light in orders of diffraction gratings of an interference linear displacement sensor," *Optics and Spectroscopy*, vol. 127, no. 3, pp. 527–534, 2019.

[44] F. A. Jenkins and H. E. White, "Fundamentals of optics," *Indian Journal of Physics*, vol. 25, pp. 265–266, 1957.

[45] D. Alj, R. Caputo, and C. Umeton, "From cartesian to polar: a new policryps geometry for realizing circular optical diffraction gratings," *Optics letters*, vol. 39, no. 21, pp. 6201–6204, 2014.

Appendix A

Mathematical derivation of the double grating diffraction

In the expression of the two-dimensional light field, the effect of each reflection grating and transmission grating wavelet is included. Using Euler's formula and geometric sequence summation formula, these items can be simplified and merged. The parameters in the expression (α, δ, γ, N, k, d, h), and simplification results have been explained in Chapter 4, here will show the mathematical derivation process in detail for readers to better understand and apply.

For the reflective grating light field E_1, the expression of each sub-wave includes two terms. The terms of the trigonometric function, $A\left[\sin\left(\alpha_1\right)/\alpha_1\right]$, represent the intensities of the light field corresponding to the diffraction angle. Since the light intensity is uniformly distributed, these terms are equal.

The exponential terms, $\exp\left[in\delta_1\right]$, represent the optical path differences caused by the relative distance from the center point. These increasing proportionally complex exponential terms can be calculated by the summation formula of a geometric sequence. Next, the calculation result is simplified into a trigonometric function using

Euler's formula, as shown in Equation (A.1).

$$
\begin{aligned}
E_1 &= A \left[\frac{\sin(\alpha_1)}{\alpha_1} \right] \cdot \left[\exp\left[i \left(-\frac{N-1}{2} \right) \delta_1 \right] + \exp\left[i \left(-\frac{N-1}{2} + 1 \right) \delta_1 \right] \right. \\
&\quad \left. + \cdots + 1 + \cdots + \exp\left[i \left(\frac{N-1}{2} \right) \right] \delta_1 \right] \\
&= A \left[\frac{\sin(\alpha_1)}{\alpha_1} \right] \cdot \left[\sum_{n=-\frac{N-1}{2}}^{\frac{N-1}{2}} \exp[in\delta_1] \right] \\
&= A \left[\frac{\sin(\alpha_1)}{\alpha_1} \right] \cdot \left[\exp\left[i \left(-\frac{N-1}{2} \right) \delta_1 \right] \cdot \frac{1 - \exp[N\delta_1]}{1 - \exp[\delta_1]} \right] \\
&= A \left[\frac{\sin(\alpha_1)}{\alpha_1} \right] \cdot \left[\exp\left[i \left(-\frac{N-1}{2} \right) \delta_1 \right] \cdot \frac{\exp\left[\frac{N}{2}\delta_1 \right] \cdot \left[\exp\left[-\frac{N}{2}\delta_1 \right] - \exp\left[\frac{N}{2}\delta_1 \right] \right]}{\exp\left[\frac{\delta_1}{2} \right] \cdot \left[\exp\left[-\frac{\delta_1}{2} \right] - \exp\left[\frac{\delta_1}{2} \right] \right]} \right] \\
&= A \left[\frac{\sin(\alpha_1)}{\alpha_1} \right] \cdot \left[\frac{\sin\left(\frac{N}{2}\delta_1 \right)}{\sin\left(\frac{\delta_1}{2} \right)} \right] \cdot \exp[i\delta_1]
\end{aligned}
$$

(A.1)

The reflector designed in this project is a movable structure with a vertical displacement relative to the grating and a rotation around the center point in the vertical plane. So in the light field expression of the transmission grating, E_2, these optical path differences are expressed as $\exp[i2k(h + x + nd\sin\gamma)]$.

Through the same simplification method as E_1, the final expression of E_2 is obtained as Equation (A.2), where $\varphi = \delta_2 + 2kd\sin\gamma$.

$$
\begin{aligned}
E_2 &= A \left[\frac{\sin(\alpha_2)}{\alpha_2} \right] \\
&\quad \cdot \left[\exp\left[i \left(-\frac{N-1}{2} \right) \delta_2 \right] \cdot \exp\left[i2k \left(h + x + \left(-\frac{N-1}{2} \right) d\sin\gamma \right) \right] \cdot \exp[i\delta_i] \right. \\
&\quad + \exp\left[i \left(-\frac{N-1}{2} + 1 \right) \delta_2 \right] \cdot \exp\left[i2k \left(h + x + \left(-\frac{N-1}{2} + 1 \right) d\sin\gamma \right) \right] \cdot \exp[i\delta_i] \\
&\quad + \cdots + \exp[i2k(h + x)] \cdot \exp[i\delta_i] + \cdots \\
&\quad \left. + \exp\left[i \left(\frac{N-1}{2} \right) \delta_2 \right] \cdot \exp\left[i2k \left(h + x + \left(\frac{N-1}{2} \right) d\sin\gamma \right) \right] \cdot \exp[i\delta_i] \right] \\
&= A \left[\frac{\sin(\alpha_2)}{\alpha_2} \right] \cdot \exp[i\delta_i] \cdot \exp[i2k(h + x)] \cdot \sum_{n=-\frac{N-1}{2}}^{\frac{N-1}{2}} \exp[in(\delta_2 + 2kd\sin\gamma)] \\
&= A \left[\frac{\sin(\alpha_2)}{\alpha_2} \right] \cdot \exp[i\delta_i] \cdot \exp[i2k(h + x)] \cdot \left[\frac{\sin\left(\frac{N}{2}\varphi \right)}{\sin\left(\frac{\varphi}{2} \right)} \right] \cdot \exp[i\varphi]
\end{aligned}
$$

(A.2)

For now, according to the superposition effect of the light field, the total light intensity corresponding to each diffraction angle can be calculated.

Programming in Matlab

This section records the codes for the numerical calculation of double grating diffraction in Matlab, which can be used for readers' reference and testing.
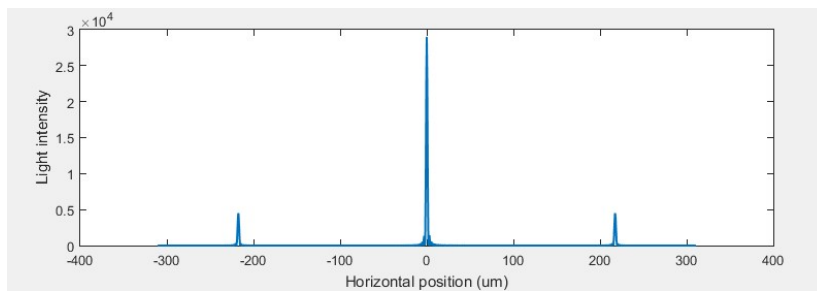
B.1 Double grating diffraction pattern

```matlab
1  clear all;
2  %Parameters setting%
3  d = 4;            %Grating period%
4  a = 2;            %Grating width%
5  h = 8;           %Initial distance between reflector and grating%
6  L = 1000;         %Working distance%
7  W = 400;          %Beam width%
8  A = 1;            %Light intensity coefficient%
9  N=fix(W/d);       %The number of grating%
10 tilt=0;           %Rotation angle%
11 lam = 0.85;       %Wave length%
12 k=2*pi/lam;       %Wave number%
13 flag=1;
14 I=zeros(1,314);
15 X=I;
16 PDI=0;
17 %Calculate the corresponding light intensity of each diffraction ...
       angle cyclically%
18 tic;
19 for thita = -0.3 :0.00001 :0.3
20     alph1=pi/lam*(d-a)*sin(thita);
21     alph2=pi/lam*a*(sin(thita)-sin(tilt));
22     derta1=2*pi/lam*d*sin(thita);
23     derta2=2*pi/lam*d*(sin(thita)-sin(tilt));
```

```
24      dertai=2*pi/lam*(d-a)*sin(thita);
25      phi=derta2+2*k*d*sin(tilt);
26      E1=A*sin(alph1)/alph1*sin(N/2*derta1)/sin(derta1/2)*exp(1i*derta1);
27      E2=A*sin(alph2)/alph2*sin(N/2*phi)/sin(phi/2)*exp(1i*phi) ...
28      *exp(1i*(dertai+2*k*h));
29      I1=abs(E1+E2)^2;
30      X1=L*tan(thita);
31      I(flag)=I1;
32      X(flag)=X1;
33      if X1 > PDl && X1 < PDr
34          PDI = PDI + I1;
35      end
36      flag=flag+1;
37  end
38  toc
39  plot(X,I,'linewidth',1.5)
40  ylabel('Light intensity')
41  xlabel('Horizontal position (um)')
```


Figure B.1: Numerical calculation results of light intensity of double grating diffraction.

B.2   Phase-shifting testing

Numerical calculation of the phase difference between the positive and negative first diffracted order light intensity changes superimposed by rotation and vertical movement.

```
1  clear all;
2  clc;
3  d = 4;
4  a = 2;
5  h = 100;
6  L = 1000;
7  W = 100;
```

```matlab
 8  A = 1;
 9  N=fix(W/d);
10  lam = 0.85;
11  k=2*pi/lam;
12  At = 0.034;
13  Ad = 30/1000;
14  PDl = 0.18*L;
15  PDr = 0.23*L;
16  PF=[];
17  for Ad = 0: 1 :50
18      Id=zeros(1,1);
19      Idd=zeros(1,1);
20      XX=0:0.001:1;
21      jj=1;
22      for t = 0 :0.001 :1
23          tilt = deg2rad(At)*sin(pi*t);
24          x = Ad/1000*cos(pi*t);
25          I=zeros(1,1);
26          X=zeros(1,1);
27          PDI=0;
28          PD0=0;
29          flag=1;
30              for thita = -0.6 :0.01 :0.6
31                  alph1=pi/lam*(d-a)*sin(thita);
32                  alph2=pi/lam*a*(sin(thita)-sin(tilt));
33                  derta1=2*pi/lam*d*sin(thita);
34                  derta2=2*pi/lam*d*(sin(thita)-sin(tilt));
35                  dertai=2*pi/lam*(d-a)*sin(thita);
36                  phi=derta2+2*k*d*sin(tilt);
37                  E1=A*sin(alph1)/alph1*sin(N/2*derta1) ...
38                  /sin(derta1/2)*exp(1i*derta1);
39                  E2=A*sin(alph2)/alph2*sin(N/2*phi)/sin(phi/2) ...
40                  *exp(1i*phi)*exp(1i*(dertai+2*k*(h+x)));
41                  I1=abs(E1+E2)^2;
42                  X1=L*tan(thita);
43                  I(flag)=I1;
44                  X(flag)=X1;
45                  if X1 > PDl && X1 < PDr
46                      PDI = PDI + I1;
47                  end
48                  if X1 > -PDr && X1 < -PDl
49                      PD0 = PD0 + I1;
50                  end
51                  flag=flag+1;
52              end
53          Id(1,jj)=PDI;
54          Idd(1,jj)=PD0;
```

```matlab
55          jj=jj+1;
56      end
57      [¬, Idmax] = max(Id);
58      [¬, Iddmax] = max(Idd);
59      PF=[PF,(XX(Idmax)-XX(Iddmax))*pi];
60      PF
61      end
62  plot([0:1:50],PF,'LineWidth',2);
63  set(gca,'linewidth',2,'fontsize',14,'FontWeight','bold')
64  xlabel('Vertical motion amplitude (nm)','FontSize',18)
65  ylabel('Phase shift (rad)','FontSize',18)
```

Vibrometer testing for the rotational movement of the mico Coriolis flow sensor

A vibrometer meter was used to detect the vibration amplitude of the mico Coriolis flow sensor and the gold-deposited silicon mirror (piezo-driven) under different voltages and frequencies.

In addition, the vibrometer can also determine the eigenfrequency of the test sample by testing the displacement response at different driving frequencies.
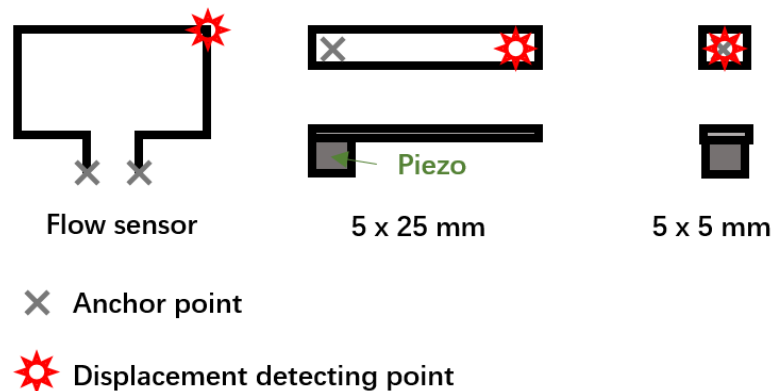
Figure C.1: Schematic diagram of test samples.

Table C.1: The test results of the flow sensor, driven by eigenfrequency (2473 Hz).

Driven voltage (V)	0.4	0.6	0.8	1.0	1.2	1.4	1.6
Amplitude (um)	9.70	14.48	19.26	23.69	28.05	32.29	36.25

Table C.2: The test results of the cantilever beam @ 2 kHz.

Driven voltage (V)	3	6	9
Amplitude (nm)	–	552.9	918.5

Table C.3: The test results of the square mirror @ 2 kHz.

Driven voltage (V)	3	6	9
Amplitude (nm)	14.75	35.63	50.37

Table C.4: The test results of the square mirror @ 2430 Hz (eigenfrequency).

Driven voltage (V)	3	6	9
Amplitude (nm)	26.30	45.64	69.82